



GEORG-AUGUST UNIVERSITÄT GÖTTINGEN

MASTER THESIS

**Numerical simulation of polygonal patterns  
in salt playa**

**Numerische Simulationen von Musterbildung  
in Salzwüsten**

prepared by

**Marcel Ernst**

from Sulingen

at the Max Planck Institute for Dynamics and Self-Organization

**First referee:** Dr. Lucas Goehring

**Second referee:** Prof. Dr. Andreas Tilgner

**Submission date:** 29th September 2017



## Abstract

In salt pans and playa we sometimes observe that salt crystallization due to evaporation forms polygonal salt ridge patterns on the surface. Ridges of crystallized salt surround a flat center with a characteristic length scale of several meters. I investigate the mechanisms driving the development of those polygonal structures as there is currently no comprehensive theory of their formation. Different approaches describing them range from wrinkling to cracking of the surface; none of these mechanisms reproduce the characteristic length scale of the pattern. Here I investigate a model that includes the subsurface dynamics of the salt water-filled porous medium below the crust: salinity gradients drive convection cells which, in turn, interact with the development of salt ridges at the surface. Firstly, I perform a linear stability analysis of the differential equations describing the dynamics of the system based on the work on Robin Wooding and extend his results by computing the neutral stability curve as well the most unstable mode for small perturbations. Secondly I use a pseudo-spectral method to implement a numerical simulation of the dynamics in the system in a simplified two-dimensional model. I compare the numerical results with the theory and experimental data in Hele-Shaw cells and investigate the feedback between surface and subsurface processes and the pinning of the subsurface convection cells to the salt ridges.

# Contents

<b>1. Introduction</b>	<b>5</b>
1.1. Motivation . . . . .	5
1.2. Outline . . . . .	7
<b>2. Theoretical Background</b>	<b>9</b>
2.1. Properties of porous media . . . . .	9
2.2. Derivation of differential equations . . . . .	10
2.3. Salinity formulation . . . . .	14
2.4. Non-dimensionalization . . . . .	15
2.5. Boundary Conditions . . . . .	17
2.6. Transient to steady-state . . . . .	18
<b>3. Investigation of stability</b>	<b>21</b>
3.1. Formulation of the problem . . . . .	21
3.2. Linear stability analysis . . . . .	22
3.3. Results . . . . .	26
<b>4. Experiments in Hele-Shaw Cells</b>	<b>29</b>
4.1. Experimental methodology . . . . .	29
4.2. Experimental Results . . . . .	31
<b>5. Double-periodic simulations</b>	<b>35</b>
5.1. Implementation . . . . .	35
5.2. Validation . . . . .	38
<b>6. Implementation of the model</b>	<b>41</b>
6.1. Differential equations . . . . .	42
6.2. Compact finite difference schemes . . . . .	45
6.3. Pseudo-spectral method . . . . .	46
6.4. Time-stepping . . . . .	48
6.5. Validation of growth rates . . . . .	49
<b>7. Results from numerical simulation</b>	<b>53</b>
7.1. Fingering behaviour . . . . .	54
7.2. Investigation of convection cells . . . . .	59
7.3. Comparision with experimental data . . . . .	63
7.4. Investigation of pinning behaviour . . . . .	66
<b>8. Summary</b>	<b>71</b>
<b>A. Appendix</b>	<b>75</b>



# 1. Introduction

## 1.1. Motivation

In salt pans and playa we sometimes observe that salt crystallization due to evaporation forms diverse polygonal salt ridge patterns on the surface. Ridges of crystallized salt surround a flat center with a characteristic length scale of several meters. In figure 2 I show examples of such structures observed in the Death Valley in California. In cooperation with Dr. Lucas Goehring and the doctoral student Jana Lasser we aim to understand the formation of those polygonal structures because there is currently no comprehensive theory of their formation. Some authors such as Tyler et al. [1] performed field studies considering the groundwater evaporation and salt flux from Owens Lake in California. Nield et al. monitored the evolution of the shapes of the salt crust patterns over time in [2].

There are two major theory to explain the evolution of the the structures ranging from wrinkling to cracking of the surface. According to the wrinkling approach the salt crust is growing over time and due to lack of space it piles up to polygonal structures [3, 4]. The alternative model implies that temperature change leads to contracting and thereby cracking of the salt crust which causes the polygons [5, 6]. Theoretical investigation of these theories enables the calculation of the expected characteristic length scales of the polygonal structures – the distance of wrinkles respectively cracks. The length scale ought to be in the order of magnitude of the thickness of the respective salt crusts [7, 8]. Since the thickness of the crust turns out to be about 1 – 15 cm while the polygonal patterns have characteristic wavelength of 1 – 3 m (measurements by Jana Lasser in the Death Valley). Hence, we state that the mentioned models are not sufficient to reproduce and explain the formation of the observed pattern.

Instead we investigate a hypothesis that includes subsurface dynamics of the porous medium saturated with salt water below the crust. We state that salinity gradients drive convection cells which, in turn, interact with the evolution of the salt ridges at the surface and have substantial impact on this process. The sand in salt playa is often saturated with salty groundwater up to a few centimeters below the surface. High temperatures due to solar radiation as well as wind enhances the evaporation of water causing the precipitation of salt and formation of a respective crust. Due to the accumulation of salt near the surface the salinity and thereby density is larger than below. If the gradient is large enough this configuration get unstable inducing the formation of convection cells in the sand. Furthermore we assume that the evaporation rate in the surrounding of the salt ridges is larger than in the flat centers which may interact with the convection cells below



(a) Length scale of patterns.

(b) Field work at Owens Lake (with Jana Lasser).

**Figure 2:** salt ridge patterns at the Owens Lake in the Death Valley, California. [Photos by Jana Lasser]

such such as pinning the up- respectively downwelling regimes to the ridges [9]. First approximations indicate that the characteristic length scales of those convection cells is presumably consistent with the observed patterns. In figure 3 I display a sketch of this model.

Jana Lasser is investigating the system experimentally using simplified two-dimensional Hele-Shaw cells to quantify the subsurface flows and is conducting field studies of the actual patterns in nature (see figure 2b. My responsibility is to increase the theoretical understanding of the system and implement a two-dimensional simulation for deeper insights.

The relevance of this project is for one thing justified by the curiosity of humans to understand natural phenomenons especially pattern formation. Besides the understanding of the dynamics of flow and convection in porous media is of significant importance: According to the International Panel on Climate Change (IPCC) the development of safe and secure mechanisms to geologically store carbon dioxide in the ground (CCS: carbon dioxide sequestration) is crucial for mitigating climate change. Carbon dioxide may be injected into deep saline aquifers where it dissolves in the ambient groundwater to remain there for centuries. [10] The solution has higher density than normal water which may lead to a convection driven by gravitational instability enhancing the rate of dissolution [11]. In addition to it the understanding of saline groundwater flow is important for the disposal of waste, e.g. radioactive waste, in geological formations, too [12].

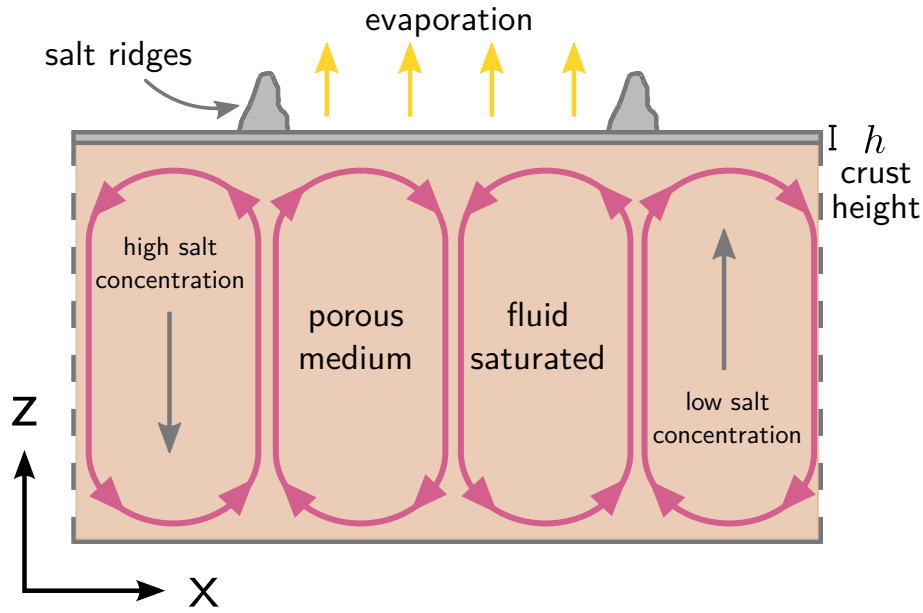


**Figure 3:** Sketch of our model including the subsurface dynamics of the porous medium saturated with salt water as well as the feedback between the formation of salt ridges at the surface and subsurface processes. Reproduced from Jana Lasser.

## 1.2. Outline

The thesis at hand is structured as follows:

In chapter 2 on the theoretical background I will introduce the properties of porous media and sketch the derivations of the differential equations describing the dynamics of the salt water flow in porous media. I show the utilized approximations and introduce a set of dimensionless differential equations using characteristic velocity and length scales of the system. I present an analytical solution of the transient behavior of the salinity at the surface following Wooding [13].

Robin A. Wooding [14] investigated – manifold unintelligible – the linear stability of a semi-infinite system with similar boundary conditions analytically. In chapter 3 I reproduce his work in detail using a semi-analytical approach and calculate the neutral stability curve of the respective system which is consistent with the results of Homsy and van Du-jin [15, 16]. Furthermore, I am able to complement their investigation by determining the most unstable mode, too.

In chapter 4 I present the experimental approach of Jana Lasser. She is performing experiments in quasi two-dimensional Hele-Shaw cells constituting a simplified model of the real-world system of salt playa, in a controlled environment. The aim of these experiments is to analyze the convective behavior in the Hele-Shaw cells. Additionally, I feature her experimental results which are later compared with the numerical simulation

to validate the latter.

As build-up for the numerical simulation of the two-dimensional salt playa system I reproduce the numerical results of Rogerson and Meiburg [17] in chapter 5. They analyzed the unstable displacement of two-dimensional flow in a porous medium under periodic boundary conditions. The set of differential equations describing the system is similar and since they assume periodicity in both directions I can use a spectral method.

In chapter 6 I present the implementation of the two-dimensional numerical model. Based on a stream function-vorticity formulation of the differential equations [18] I utilize a pseudo-spectral method to solve the Poisson equation following the approach of Ruith and Meiburg [19], Riaz and Meiburg [20] and Chen [21] since I assume periodicity in only one direction. To compute the derivatives I use compact finite difference schemes [22] and integrate the equations with Runge-Kutta time-stepping [23]. I validate the implementation using the linear stability analysis.

Using this numerical simulation I present results in chapter 7. Firstly, I consider the early-time such as the fingering behavior. I investigate the wavelength and velocity scales of the occurring convection cells to compare the results with the experimental data. Furthermore, I look at the feedback mechanisms between variations in evaporation rate at the surface and the subsurface convection cells such as pinning. This helps to check the plausibility of the convection hypothesis.

Finally, I will summarize the main results in chapter 8.

## 2. Theoretical Background

In this chapter I sketch the derivation of the differential equations governing the dynamics of the flow of salty fluids in porous media: Analogous to [12] I formulate the conservation equations for mass, salt concentration and momentum. Besides the assumption of non-compressibility and the advection diffusion equation for salty fluids I make use of the *Darcy Law* formulated by Henry Darcy in 1856 [24] describing the momentum conservation of a fluid in a porous medium.

Furthermore, I derive a dimensionless set of differential equations based on characteristic length and time scales of the system. Assuming that the solute (salt) modifies the solvent density weakly, I apply the Boussinesq approximation and present the imposed boundary conditions in the salt playa system and present the analytical solution done by Wooding in 1997 [13] of the stable transient in case there is no crust on the surface and uniform up-flow of salty water.

### 2.1. Properties of porous media

Figure 4 displays an exemplary two-dimensional slice of sandstone displaying the high complexity and tortuosity of such rocks as well as its fluid dynamics. Considering the porous medium on a microscopic length scale one needs to show consideration for the heterogeneous structure of the single pores that influence the pathway of the flows. Despite that heterogeneity a porous medium often can be considered as a homogeneous on a macroscopic length scale and has universal macroscopic properties which are spatially independent. Since it is usually sufficient to analyze the flow on a length scales much larger than the size of single pores, we need to characterize the macroscopic differential equations governing the dynamics. [25] I only consider porous media saturated with fluid in order that the space between the pores is occupied by the fluid phase rather than for example by air.

For that purpose I consider three basic parameters to describe the macroscopic properties of a porous medium. The porosity  $\phi$  is the ratio of the void volume to the total volume of the porous medium. [26]

The superficial flow velocity  $\mathbf{q} = \phi \mathbf{v}$  in porous media, with microscopic advection velocity  $\mathbf{v}$ , is described by the *Darcy law*

$$\mathbf{q} = -\frac{\kappa}{\mu} \cdot \nabla p.$$

Here  $\nabla p$  is the pressure gradient,  $\mu$  the viscosity of the fluid and  $\kappa$  the permeability.

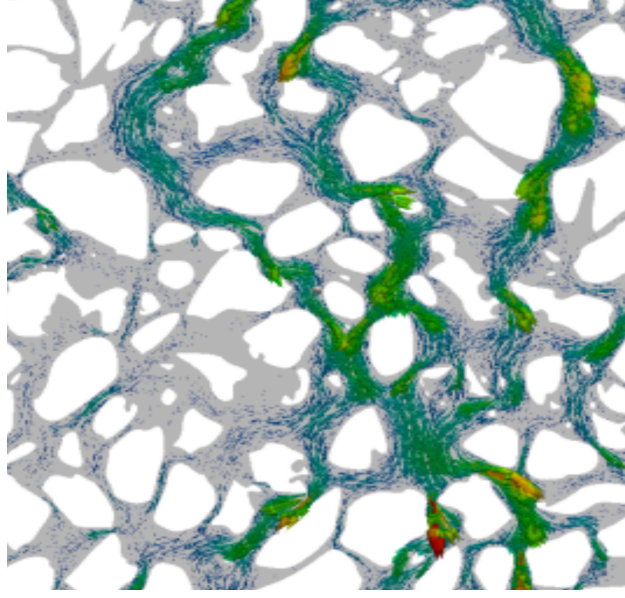


**Figure 4:** Two-dimensional slice of sandstone in the length scale of the pores visualizing the flow of a fluid through a porous medium. Reproduced from [25].

In general the permeability  $\kappa$  is a tensor of second-order but in case of isotropic porous media, this can safely be assumed for sand, it simplifies to a scalar constant  $\kappa$  usually expressed in units of  $\text{m}^2$ . It is a property of the geometry of the medium. Typical values for sand are about  $\varphi \approx 0.37 \dots 0.50$  and  $\kappa \approx 2 \times 10^{-7} \dots 1.8 \times 10^{-6} \text{m}^2$ [26].

## 2.2. Derivation of differential equations

To analyze the mass and salt conservation of salty fluid in a porous medium I start by writing down equations at the scale of the individual pores and average those equations over representative elementary volumes (REV)  $V_{\text{REV}} =: (l_{\text{REV}})^3$  much larger than the pore length scale  $l_p$  and much smaller than the system size  $L$ :  $l_p \ll l_{\text{REV}} \ll L$ . Then I use weighted averages over the different species (water and concentrated salt solution) and sketch the derivation the continuous porous media equations. The following notation and derivation is based on the work of Herbert et al. [12]

### 2.2.1. Mass conservation

I consider mass conservation in the system of salt and water within the porous medium and look on the salt water as a mixture of fresh water (species  $\alpha = 1$ ) and a concentrated salt solution (species  $\alpha = 2$ ). I introduce the mass fraction  $\omega_\alpha$  of each liquid species  $\alpha$  in this mixture and moreover define  $c_m := \omega_2$ . Hence,  $\omega_1 = 1 - c_m$ .  $c_m = 1$  represents

saturated salt water and  $c_m = 0$  fresh water. The density conservation equation for each species is given by

$$\frac{\partial \rho_\alpha^{\text{pore}}}{\partial t} + \nabla \cdot (\rho_\alpha^{\text{pore}} \mathbf{v}_\alpha^{\text{pore}}) = 0 \quad (2.1)$$

whereby  $\rho_\alpha^{\text{pore}}$  and  $\mathbf{v}_\alpha^{\text{pore}}$  are the density and the partial, advective velocity of the fluid species  $\alpha$  in the length scale of the pores.

To average over a representative volume  $V_{\text{REV}}$  containing many individual pores we are using the density-weighted averages

$$\begin{aligned} \rho_\alpha &= \frac{1}{V_{\text{REV}}} \int_{V_{\text{REV}}} \rho_\alpha^{\text{pore}} dV, \\ \mathbf{v}_\alpha &= \frac{\int_{V_{\text{REV}}} \rho_\alpha^{\text{pore}} \mathbf{v}_\alpha^{\text{pore}} dV}{\int_{V_{\text{REV}}} \rho_\alpha^{\text{pore}} dV}. \end{aligned}$$

with the partial densities  $\rho_\alpha$  of the two species given by

$$\overline{\rho_\alpha} = \varphi \rho \omega_\alpha.$$

Here,  $\varphi$  is the porosity of the porous medium and assumed to be a constant.  $\rho$  is the actual density of the fluid and  $\omega_\alpha$  the mass fraction of each species. We know that  $\omega_2 = c_m$  and hence  $\omega_1 = 1 - c_m$ .

By averaging equation (2.1) over the representative volume we get with continuity and differentiability of  $\rho_\alpha^{\text{pore}}$  and  $\mathbf{v}_\alpha^{\text{pore}}$

$$\begin{aligned} &\frac{1}{V_{\text{REV}}} \int_{V_{\text{REV}}} \left[ \frac{\partial \rho_\alpha^{\text{pore}}}{\partial t} + \nabla \cdot (\rho_\alpha^{\text{pore}} \mathbf{v}_\alpha^{\text{pore}}) \right] dV = 0, \\ \Rightarrow \quad &\frac{\partial}{\partial t} \left( \frac{1}{V_{\text{REV}}} \int_{V_{\text{REV}}} \rho_\alpha^{\text{pore}} dV \right) + \nabla \cdot \left( \frac{1}{V_{\text{REV}}} \int_{V_{\text{REV}}} \rho_\alpha^{\text{pore}} \mathbf{v}_\alpha^{\text{pore}} dV \right) = 0, \\ &\Rightarrow \quad \frac{\partial \rho_\alpha}{\partial t} + \nabla \cdot (\rho_\alpha \mathbf{v}_\alpha) = 0 \quad (2.2) \end{aligned}$$

involving a mass flux of  $\rho_\alpha \mathbf{v}_\alpha$ .

We now average equation (2.2) over the two species  $\alpha = 1, 2$  using the overall advective velocity

$$\mathbf{v} = \frac{\sum_{\alpha=1}^2 \rho_\alpha \mathbf{v}_\alpha}{\sum_{\alpha=1}^2 \rho_\alpha}$$

as well as the porosity adjusted Darcy or superficial velocity  $\mathbf{q} = \varphi \mathbf{v}$  to get

$$\begin{aligned} \sum_{\alpha=1}^2 \left[ \frac{\partial \rho_{\alpha}}{\partial t} + \nabla \cdot (\rho_{\alpha} \mathbf{v}_{\alpha}) \right] &= 0, \\ \left( \sum_{\alpha=1}^2 \frac{\partial \rho_{\alpha}}{\partial t} \right) + \nabla \cdot \left( \sum_{\alpha=1}^2 \rho_{\alpha} \mathbf{v}_{\alpha} \right) &= 0, \\ \varphi \frac{\partial \rho}{\partial t} + \nabla \cdot (\rho \mathbf{q}) &= 0. \end{aligned} \quad (2.3)$$

### 2.2.2. Salt conservation

We consider salt conservation in the system and express the total flux of the saline species  $\alpha = 2$  as the sum of the advective and the diffusive flux

$$\rho_2 \mathbf{v}_2 = \rho_2 \mathbf{v} + \mathbf{j}_2 = \rho_2 \mathbf{v} - \varphi \rho \mathbf{D} \cdot \nabla c_m.$$

Here,  $\mathbf{D}$  is the hydrodynamic diffusion-dispersion tensor. Mechanical dispersion is assumed to be much smaller than molecular diffusion for the relevant length scales in our system (compare [13, 27]). For analyzing experimental data I will check whether this condition is fulfilled. Hence, I neglect the dispersion contribution and only take into account the molecular diffusion  $D$  which is a scalar and independent of space.

Plug in that relation in equation (2.2) for saturated salt solution ( $\alpha = 2$ ) and using the relation  $\rho_2 = \varphi \rho \omega_2 = \varphi \rho c_m$  we get

$$\begin{aligned} \frac{\partial \rho_2}{\partial t} + \nabla \cdot (\rho_2 \mathbf{v} - \varphi \rho \mathbf{D} \cdot \nabla \omega_2) &= 0, \\ \frac{\partial \rho c_m}{\partial t} + \nabla \cdot (\rho c_m \mathbf{v}) - \nabla \cdot (\rho \mathbf{D} \cdot \nabla c_m) &= 0. \end{aligned} \quad (2.4)$$

Assuming incompressibility  $\nabla \cdot \mathbf{v} = 0$  and  $\mathbf{D} = D \mathbf{1}$  it simplifies to

$$\frac{\partial \rho c_m}{\partial t} + \mathbf{v} \cdot \nabla (\rho c_m) - D \nabla \cdot (\rho \nabla c_m) = 0. \quad (2.5)$$

### 2.2.3. Darcy Law

The basic equation to describe the momentum balance of fluid in porous media is the *Darcy Law* which firstly was formulated by Henry Darcy in 1856 in [24]. He used an experimental method to obtain the proportional relation between the flow rate in a porous medium and the total pressure drop across it. In 1937 Muskat presented the general



expression [28] in the simplest form

$$q = -\frac{\kappa}{\mu} \nabla p$$

with a intrinsic material parameter, the permeability  $\kappa$ , and the mass flow rate respectively the superficial velocity  $q$ . The equation holds on length scales much larger than pores and smaller then the macroscopic size of the system. Since a rigorous analytical derivation of the Darcy Law is quite challenging I will only depict the underlying assumptions.

Based on the Navier-Stokes equation describing the dynamics of fluid flows there are several derivations, for example Neuman in 1977 [29].

To derive the Darcy Law one has to assume a stationary solid phase of porous media and a creeping flow which has the property that the drag forces are much larger than inertial forces corresponding to a low Reynold number ( $\text{Re} \lesssim 1$ ). Hence, we can neglect the inertial term in the Navier-Stokes equation to get the Stokes equation in the fluid

$$-\nabla p + \mu \nabla^2 \mathbf{q} + \mathbf{f} = 0$$

with external forcing  $\mathbf{f}$  such as gravity. Additionally we have to assume incompressibility of the fluid  $\nabla \cdot \mathbf{q} = 0$  and no-slip boundary conditions for the boundaries between the solid and the fluid:  $\mathbf{q}|_{\text{boundary}} = 0$ . [30]

Whitaker derived the Darcy law using the method of volume averaging respectively mean-field approximation [31]. The validity is again based on the restriction that the length scale of the representative volume elements is much smaller than the sample size:  $l_{\text{REV}} \ll L$ . The porous medium does not need to be homogeneous or periodic but abrupt structural changes are not considered [31]. Other authors make use of the homogenization method assuming periodic and regular patterns in the REV [30, 32].

Brinkman presented a generalized form of the Darcy Law without neglecting the dissipative viscous term of the Navier-Stokes equation for larger Reynold numbers [33].

Assuming that the porous medium is a collection of spheres with constant radius  $r_{\text{particles}}$  and a porosity of  $\varphi$  the *Carman–Kozeny equation* gives a relation to calculate the permeability  $\kappa$

$$\kappa = r_{\text{particles}}^2 \frac{\varphi^3}{45(1 - \varphi)^2}. \quad (2.6)$$

as given in [34]. This relation enables one to estimate the permeability of sand with a given particle radius.

In case the system is affected by gravity  $\mathbf{g}$  we can adjust the Darcy Law

$$\mathbf{q} = \varphi \mathbf{v} = -\frac{\kappa}{\mu} (\nabla p - \rho \mathbf{g}) \quad (2.7)$$

with the buoyancy term  $\mathbf{f} = \rho \mathbf{g}$ . [12]

### 2.3. Salinity formulation

According to Herbert et al.[12] the density of saline water  $\rho = \rho(c_m)$  fulfills the condition

$$\frac{1}{\rho(c_m)} = \frac{c_m}{\rho_s} + \frac{1 - c_m}{\rho_0} \quad (2.8)$$

with density of fresh water  $\rho_0$  and saturated salt water  $\rho_s$  if we assume that the volumes of the two species are additive which is equivalent to reciprocal additivity of density.

In figure 5a I compare this relation with the actual empirical values for the density dependence  $\rho(c_m)$  from Weast 1977 [35]. It shows that this is a reasonable good fit. Under this assumption we can express the differential equations using the density adjusted fraction  $c_v$  of the saline phase instead of the mass fraction  $c_m$

$$c_v := \frac{\rho c_m}{\rho_s} = \frac{\rho - \rho_0}{\rho_s - \rho_0}.$$

The latter is a consequence of equation (2.8). With this we can express – analogous to Herbert et al. [12] – the salt conservation (2.4) as

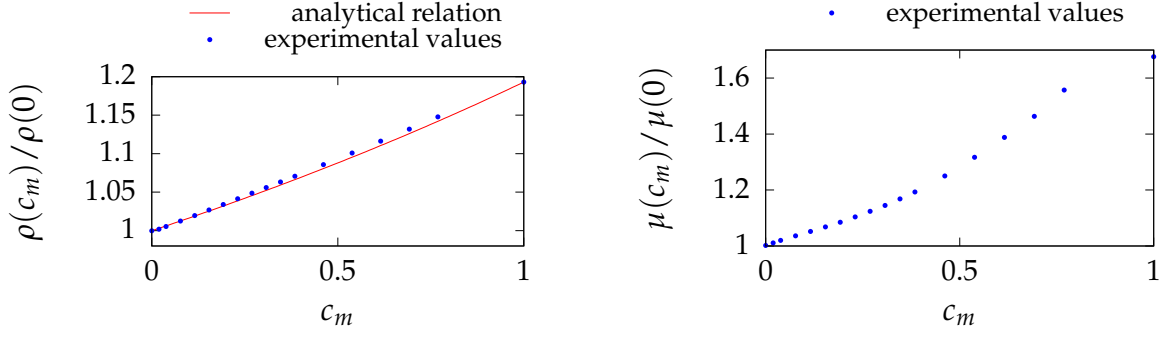
$$\varphi \frac{\partial c_v}{\partial t} + \nabla \cdot (c_v \mathbf{q}) - D \varphi \nabla \cdot \left( \frac{\rho_0}{\rho} \nabla c_v \right) = 0.$$

Assuming a background density  $\rho_b$  and a maximal density  $\rho_m$  of salty water with  $\rho_s \geq \rho_m > \rho_b \geq \rho_0$  we can define the relative salinity

$$S := \frac{\rho - \rho_b}{\rho_m - \rho_b} = \frac{\rho - \rho_b}{\Delta \rho} \Rightarrow \rho = S \Delta \rho + \rho_b$$

with  $\Delta \rho = \rho_m - \rho_b$  and the background salinity

$$S_b := \frac{\rho_b - \rho_0}{\rho_m - \rho_b} = \frac{\rho_b - \rho_0}{\Delta \rho} \Rightarrow S + S_b = \frac{\rho - \rho_0}{\Delta \rho} = c_v \frac{\rho_s - \rho_0}{\Delta \rho}. \quad (2.9)$$



(a) Density  $\rho(c_m)$  based on empirical data [35] and the analytical relation (2.8).

(b) Viscosity  $\mu(c_m)$  based on empirical data [35].

**Figure 5:** Density and viscosity of salt water as a function of the mass fraction of saturated salt solution  $c_m$  for a temperature of 20 °C.  $c_m = 1$  represents saturated salt water while  $c_m = 0$  corresponds to fresh water.

For constant porosity  $\varphi$ , diffusion  $D$  and permeability  $\kappa$  we can express the equations as

$$\begin{aligned}\varphi \frac{\partial \rho}{\partial t} + \nabla \cdot (\rho \mathbf{q}) &= 0, \\ \varphi \frac{\partial S}{\partial t} + \nabla \cdot (S \mathbf{q}) &= D \varphi \nabla \cdot \left( \frac{\rho_0}{\rho} \nabla S \right), \\ \mathbf{q} &= -\frac{\kappa}{\mu} \nabla p - \frac{\kappa \mathbf{g}}{\mu} (S \Delta \rho + \rho_b).\end{aligned}$$

I now take advantage of the Boussinesq approximation that the density dependence is only considered in the buoyancy term in the Darcy Law and neglected in the diffusional term ( $\rho_0/\rho \approx 1$ ) and the mass conservation equation which reduces to incompressibility. The constant background density is absorbed into the pressure term using the vertical height  $z$ . Hence, the equations read

$$\begin{aligned}\nabla \cdot \mathbf{q} &= 0, \\ \varphi \frac{\partial S}{\partial t} + \mathbf{q} \cdot \nabla S &= D \varphi \nabla^2 S, \\ \mathbf{q} &= -\frac{\kappa}{\mu} \nabla (p - \rho_b g z) - \frac{\kappa \mathbf{g}}{\mu} (S \Delta \rho + \rho_b).\end{aligned}$$

## 2.4. Non-dimensionalization

For further investigation of the system I will non-dimensionalize the governing equations. For that purpose I make use of the natural velocity scale  $E_0$  (e. g. the mean evapo-

ration rate) to introduce the length and time scales

$$L = \frac{D}{E_0}, \quad T = \frac{D}{E_0^2}.$$

The length scale  $L$  corresponds to the distance over which advective and diffusive effects have the same order of magnitude and  $T$  is the characteristic time for the advective respectively diffusive flow to travel the distance  $L$ .

I define the adjusted dimensionless pressure which includes the absorbed term of constant background density

$$P := (p - \rho_b g z) \frac{\kappa}{\varphi \mu D},$$

the dimensionless time  $\tau$ , space  $X, Y, Z$  as well as the velocity vector

$$\mathbf{U} := \frac{\mathbf{q}}{\varphi E_0}.$$

I now have the non-dimensionalized set of differential equations

$$\nabla \cdot \mathbf{U} = 0, \tag{2.10}$$

$$\frac{\partial S}{\partial \tau} + \mathbf{U} \cdot \nabla S = \nabla^2 S, \tag{2.11}$$

$$\mathbf{U} = -\nabla P - Ra S \hat{Z} \tag{2.12}$$

with the dimensionless Rayleigh number

$$Ra := \frac{\kappa \Delta \rho g}{\varphi \mu E_0}. \tag{2.13}$$

The Rayleigh number describes the ratio of buoyancy and dissipative effects and is constant for the fluid if I assume the viscosity  $\mu = \mu(\rho)$  to be constant itself. The Rayleigh number describes the buoyancy instability of the system and if exceeding a certain threshold  $Ra_c$  instability will occur. By including the porosity  $\varphi$  in the scaling of the velocity and the pressure as well in the Rayleigh number I can eliminate this constant number in the differential equations. The Peclet number of the advective transport is  $Pe = \frac{E_0 L}{D} = 1$ . Hence, the Peclet number is not a system parameter but a constant by definition.

In figure 5b I display the change of the viscosity as a function of the mass concentration of saturated water  $c_m$ . Although the viscosity varies about 65% I assume it to be constant  $\mu = \mu(\rho_0)$  to simplify the theoretical and numerical model since it does not alter the

results significantly [13]. For subsequent work it is interesting to analyze the effects of these variations.

## 2.5. Boundary Conditions

Depending on the physical conditions various boundary conditions at the surfaces of the porous medium are possible. We presume the porous medium is occupying the half-space for  $Z \leq 0$ : a semi-infinite system with a horizontal surface. If we have ponding water at the surface or a system saturated with fluid up to the surface the pressure  $P_m$  as well as the salt concentration is constant. Hence, XYZ the density  $\rho_m$  at  $Z = 0$  is constant. [13]

Our focus will be on saturated, dry salt playa with evaporating water at the surface. The latter is driven by external energy input such as solar radiation. The evaporation rate can thus vary as  $E(X, Y, \tau)$  in space and time. Here, we assume the velocity to be normal ( $\hat{Z}$ -direction) to the boundary and in first approximation to be constant at the surface:  $U_Z(Z = 0) = q/E_0 = 1$ . Variations due to soil and atmospheric properties are taken to be small enough to be neglected. In case of already formed salt ridge patterns the vertical evaporation rate may vary in the surrounding of those structures. These variations *might* effect the position of the convection cells beneath the surface by pinning their up- or downwelling. This effect is studied in section 7.4 using numerical simulations.

Due to the evaporation of water at the surface, salt will accumulate there. After saturation is reached at the top the salt will have to precipitate atop the porous medium boundary and a salt crust forms. Hence, the salt exits the porous medium and the salt in the crust has no direct effect on the dynamics of the flow anymore. The boundary condition then is

$$\rho(Z = 0) = \rho_s = \rho_m \quad \Rightarrow \quad S = 1.$$

If the salt concentration at the surface is below saturation I assume that no salt is crossing the boundary and no salt crust will evolve. The upward advective flux at that surface of the salt will balance the downward diffusive flux (1st Ficks Law)[13]:

$$E c_v = \frac{\partial c_v}{\partial z} \quad \Rightarrow \quad S + S_b = \frac{\partial S}{\partial Z}. \quad (2.14)$$

For  $Z \rightarrow -\infty$  I will suppose a background density  $\rho_b$  and hence  $S \rightarrow 0$ . In case we have a system with finite height  $H$  in vertical direction these will be the presumed boundary conditions for  $Z = -H$ . In the two-dimensional simulations I will simplify the system

by eliminating one horizontal dimension making use of periodic boundary conditions in horizontal  $X$ -direction. The Rayleigh number  $Ra$  and the height  $H$  are a full set of parameters to characterize this system.

## 2.6. Transient to steady-state

In the following I investigate the development of such a porous medium in half-space ( $Z \leq 0$ ) saturated with salt water of background density  $\rho = \rho_b$  respectively a salinity of  $S = 0$  and assume the water evaporating with a uniform flow rate at the surface,  $E(X,Y,\tau) = E_0$ , and analyze the transient until the salt concentration near the surface reaches the maximum ( $\rho = \rho_s$  corresponding  $S = 1$ ) at time  $\tau_s$ . During this period no salt will cross the surface and the boundary condition (2.14) can be applied. For  $z \rightarrow -\infty$  we have  $S \rightarrow 0$  since we assume water of background density coming from below.

For that purpose I consider a system with neither disturbance nor convection rolls and reduce the set differential equations to a one-dimensional advection diffusion equation since gradients in horizontal direction vanish. In that case the non-dimensional vertical velocity is constant  $U_Z(X,Y,Z,\tau) = 1$ . I describe the salt conservation (2.11) as

$$\frac{\partial S}{\partial \tau} + \partial_Z S = \partial_Z^2 S.$$

Wooding gives an analytical solution of this problem in [13] for  $0 \leq \tau \leq \tau_s$  as follows:

$$S(Z,\tau) = S_b e^{Z/2} \left[ \frac{\tau + Z + 1}{2} e^{Z/2} \operatorname{erfc} \left( -\frac{\tau + Z}{2\sqrt{\tau}} \right) - \frac{1}{2} e^{-Z/2} \operatorname{erfc} \left( \frac{\tau + Z}{2\sqrt{\tau}} \right) + \sqrt{\frac{\tau}{\pi}} \exp \left( -\frac{Z^2 + \tau^2}{4\tau^2} \right) \right].$$

In figure 6 I display the salinity  $S(Z)$  for different times  $\tau \leq \tau_s$ . We clearly see that the length scale of the (approximately exponential) distribution is increasing.

At saturation time  $\tau_s$  we fulfill the boundary condition  $S = 1$  at  $Z = 0$  which is than fixed because salinity cannot be larger. The steady-state solution of the system now is given by

$$S^0(Z \leq 0) = e^Z.$$

In figure 7 I display the increasing salinity at the surface  $S(Z = 0, \tau)$  for  $\tau \leq \tau_s$  in units of background salinity  $S_b$ . I will later use this analytical solution to validate the numerical simulation with experimental data.

In later described experiments Jana Lasser uses saline water with 2.5 g salt per 1 kg water

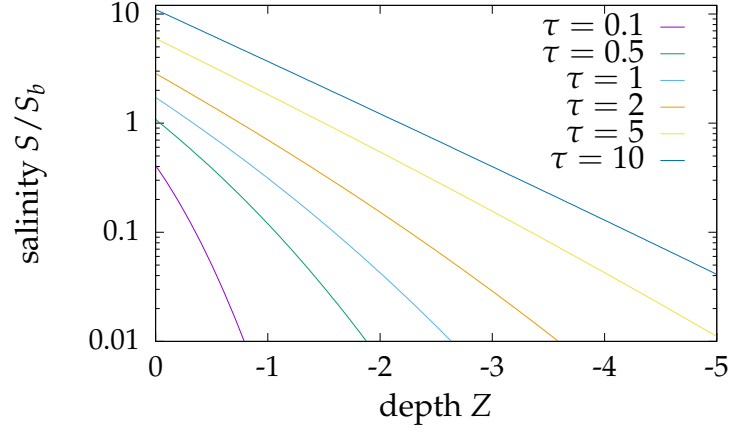


**Figure 6:** Logarithmic salinity  $S(Z)$  in units of  $S_b$  for different times  $\tau$  before saturation at surface if  $\tau \leq \tau_s$  at that time.

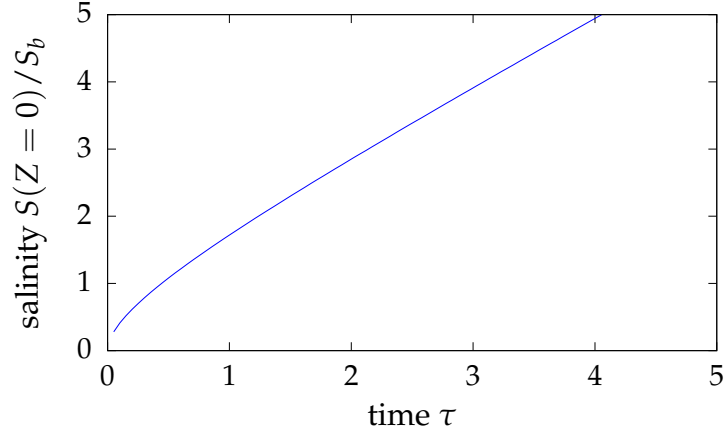


**Figure 7:** Salinity  $S(Z = 0, \tau)$  in units of  $S_b$  at the surface before it reaches saturation at the surface.

which corresponds to a background salinity of  $S_b = 1/14.2 \approx 7.04 \cdot 10^{-2}$ . Solving for  $S(Z = 0, \tau_s) = 1$ , we get  $\tau_s \approx 13.2$  applying these values.





### 3. Investigation of stability

To get a quantitative and a qualitative understanding of the conditions in our proposed system leading to a buoyancy-driven instability there is need to perform a linear stability analysis. This is the foundation to check the consistency of the numerical and experimental results and acquire a deeper understanding of the conditions of stability in the salt playa system. In 1960 Robin Wooding performed a linear stability analysis for a system with an equivalent set of differential equations describing the temperature in a semi-infinite, three-dimensional porous medium with a permeable surface covered with a cold fluid. In contrast to Wooding we are focusing on the dynamics of salty water in porous media with evaporation of water at the surface. In his analytical work he accomplishes a calculation of the critical Rayleigh number and the neutral stability curve as a function of the characteristic wave-number of the disturbance and the Rayleigh number. [14] In 1976 Homsy [15] computed the critical point for our system and in 2002 van Duijn used an energy minimization method to compute the neutral stability curve [16]. In addition to their work I am able to compute the most unstable mode of the system.

Trying to reconstruct the derivations of Wooding I experienced difficulties which I were not able to dissolve completely because his derivations are incomplete and described opaque. Nonetheless I reproduce the theoretical results of Wooding with an approach which is semi-analytical with numerical calculations using Mathematica. In addition to reproducing his findings I calculate the growth rate of disturbances as a function of the Rayleigh number and the wave-number beyond neutral stability. In consequence this allows one to compute the most unstable wavelength for a given Rayleigh number. Besides I can produce solutions to a problem with the boundary conditions which we assume for our system: uniform evaporation rate at the surface.

In the following I use the earlier established notation and the non-dimensionalized equations for salt gradient driven instability instead of temperature. Wooding utilizes the Boussinesq approximation assuming that the density  $\rho$  depends linearly on the temperature and the diffusivity. He further assumes that the specific heat is spatially invariant which corresponds to uniform diffusion  $D$ . Wooding does explore the effect of constant viscosity ( $\mu = \mu(\rho_0)$ ) at the end of his calculation.

#### 3.1. Formulation of the problem

For my derivation I will use the non-dimensionalized equations as given in (2.10), (2.11) and (2.12) in a porous-medium filling the half-space for  $0 \geq Z \geq -\infty$  which

- I) is covered by a liquid of constant density  $\rho = \rho_m$  (salinity  $S = 1$ ) at  $Z = 0$  and

constant dimensionless pressure  $P|_{Z=0} = P_m$ . This boundary condition is used by Wooding in [14].

II) has a constant density  $\rho = \rho_m$  (salinity  $S = 1$ ) at  $Z = 0$  as well as a uniform vertical evaporation rate  $\mathbf{u}|_{Z=0} = 1 \hat{\mathbf{Z}}$ . This boundary condition is later used in the investigation of salt playa for  $\tau \geq \tau_s$ .

For both top boundary conditions I presume an uprising flow from an infinitely far-away source at  $Z = -\infty$  with background density  $\rho_b$  ( $S = 0$ ). In steady-state we therefore have a uniform velocity  $\mathbf{U}^0 = 1 \hat{\mathbf{Z}}$  (unit vector in  $Z$ -direction) in positive  $Z$ -direction, the salinity  $S^0(Z) = e^Z$  and the pressure  $P^0(Z)$ .

### 3.2. Linear stability analysis

To investigate the stability of the steady-state, I consider small perturbations of the the salinity, pressure and velocity relative to the steady-state:  $\tilde{S} = S - S^0$ ,  $\tilde{P} = P - P^0$  respectively  $\tilde{\mathbf{U}} = \mathbf{U} - \mathbf{U}^0$ . After linearizing I obtain

$$\nabla \cdot \tilde{\mathbf{U}} = 0, \quad (3.1)$$

$$\begin{aligned} \frac{\partial \tilde{S}}{\partial \tau} + \mathbf{U}^0 \cdot \nabla \tilde{S} + \tilde{\mathbf{U}} \cdot \nabla S^0 - \nabla^2 \tilde{S} &= 0, \\ \Rightarrow \frac{\partial \tilde{S}}{\partial \tau} + \frac{\partial \tilde{S}}{\partial Z} + \tilde{w} \frac{\partial S^0}{\partial Z} - \nabla^2 \tilde{S} &= 0. \end{aligned} \quad (3.2)$$

$$\nabla \tilde{P} + Ra \tilde{S} \hat{\mathbf{Z}} + \tilde{\mathbf{U}} = 0, \quad (3.3)$$

using  $\tilde{w} := \hat{\mathbf{Z}} \cdot \tilde{\mathbf{U}}$ , the  $Z$ -direction of  $\tilde{\mathbf{U}}$ , as well as  $\mathbf{U}^0 = \hat{\mathbf{Z}}$ . The two inner terms in (3.2) only considers the  $Z$ -direction because the steady-state solution only depends on this direction.

To eliminate the pressure perturbations  $\tilde{P}$  and the horizontal components of  $\tilde{\mathbf{U}}$  I rearrange equation (3.3) with  $\mathbf{T}^{\text{lh}} := \nabla \tilde{P} + Ra \tilde{S} \hat{\mathbf{Z}} + \tilde{\mathbf{U}} = 0$  by applying

$$\nabla^2 T_Z^{\text{lh}} - \partial_Z (\nabla \cdot \mathbf{T}^{\text{lh}}) = 0$$

and (3.1) as well as the notation  $\nabla_1^2 := \nabla^2 - \partial_Z^2 = \partial_X^2 + \partial_Y^2$  to get

$$\nabla^2 \tilde{w} + Ra \nabla_1^2 \tilde{S} = 0. \quad (3.4)$$

Utilizing equation (3.2) I get the relation

$$\tilde{w} = \left( \frac{\partial S^0}{\partial Z} \right)^{-1} \left( \nabla^2 \tilde{S} - \frac{\partial \tilde{S}}{\partial Z} - \frac{\partial \tilde{S}}{\partial \tau} \right). \quad (3.5)$$

- I) Assuming uniform pressure and salinity at the top boundary I can set the pressure and salinity perturbation  $\tilde{P}(Z=0) = 0$  and  $\tilde{S}(Z=0) = 0$ . Hence, I know

$$\partial_X \tilde{P} \Big|_{Z=0} = \partial_Y \tilde{P} \Big|_{Z=0} = 0.$$

Using (3.3) it follows that the central term and the  $X/Y$ -components of the velocity perturbation  $\tilde{\mathbf{U}}$  vanish and only  $\tilde{w} := \hat{\mathbf{Z}} \cdot \tilde{\mathbf{U}}$  remains. Equation (3.1) yields

$$\partial_Z \tilde{w} \Big|_{Z=0} = 0.$$

- II) For uniform evaporation rate and salinity at the top boundary I can set  $\tilde{S}(Z=0) = 0$  as well as  $\tilde{w}(Z=0) = 0$ . The latter is known by definition if the vertical velocity perturbation vanish.

For both top boundary conditions the vertical perturbation of the velocity  $\tilde{w}$  vanishes for  $Z \rightarrow -\infty$ . Utilizing equation (3.5) and  $\frac{\partial S^0}{\partial Z} = e^Z$  I conclude that the denoted derivatives of  $\tilde{S}$  have to decay faster than  $e^Z$  for  $Z \rightarrow -\infty$ ,  $e^Z \frac{\partial \tilde{S}}{\partial Z} \rightarrow 0$ . Otherwise  $\tilde{w} \rightarrow 0$  could not be fulfilled. Hence, we have the condition for the bottom boundary  $Z \rightarrow -\infty$

$$\tilde{w} \rightarrow 0 \quad \Rightarrow \quad e^Z \frac{\partial \tilde{S}}{\partial Z} \rightarrow 0. \quad (3.6)$$

The perturbations fulfill the boundary conditions. Now I use the instability  $\tilde{S}(X,Y,Z,\tau)$  given by Pellew and Southwell in 1940 [36] following the approach of Wooding which separates the variables

$$\tilde{S}(X,Y,Z,\tau) = F(Z)\Phi(X,Y) \exp(\Omega\tau). \quad (3.7)$$

I assume that  $\Phi = \Phi(X,Y)$  satisfies  $(\nabla_1^2 + a^2)\Phi(X,Y) = 0$  whereby  $a$  is the characteristic wavenumber of the perturbations in horizontal  $X$ - and  $Y$ -direction.  $F(Z)$  is the most unstable perturbation of the vertical salinity field and  $\Omega$  its non-dimensional growth rate. For  $\Omega > 0$  the amplitude of the perturbation increases and hence the system is unstable and for  $\Omega < 0$  the perturbation decays and the system is stable.

For later investigation of the numerical simulation as well as the experiments in Hele-

Shaw cells – both representing a two-dimensional system – I note that eliminating the  $Y$ -direction does not alter the following analytical results. In that case we have  $\Phi = \Phi(X)$  and assume the relation  $(\partial_X^2 + a^2)\Phi(X) = 0$  for the horizontal dependence of the perturbation.

Using (3.5) I plug in the perturbation (3.7) in (3.4) to get the eigenvalue equation for the non-dimensional height-dependence  $F(z)$

$$(\partial_Z^2 - a^2 \partial_Z) e^{-Z} (\partial_Z^2 - \partial_Z - a^2 - \Omega) F(Z) = a^2 Ra F(Z). \quad (3.8)$$

According to the relation for the Rayleigh number (2.13) the system is only affected by gravitational instability.

I) In case of a top boundary condition of constant pressure I define

$$G(Z) := \left( \partial_Z \left[ e^{-Z} (\partial_Z^2 - \partial_Z - a^2 - \Omega) \right] F(Z) \right) \quad (3.9)$$

and using (3.5), the perturbation function (3.7) and the boundary condition

$$\left. \frac{\partial \tilde{w}}{\partial Z} \right|_{Z=0} = 0 \text{ rearranges to } G(Z=0) = 0.$$

II) In case of uniform evaporation rate I introduce

$$G(Z) := \left[ \partial_Z^2 - \partial_Z - a^2 - \Omega \right] F(Z) = 0 \quad (3.10)$$

and likewise get the condition  $G(Z=0) = 0$  because  $\tilde{w}(Z=0) = 0$ .

Besides we have  $F(Z=0) = 0$  in both cases due to  $\tilde{S}(Z=0) = 0$ .

Using the Mathematica tool DSolve I obtain an analytical solution of the differential equation (3.8) operating on  $F(Z)$ . The solution is a superposition of four independent infinite series solutions with eigenvalues of

$$\begin{aligned} c_{0/1} &= 1 \pm a \\ c_{2/3} &= \frac{1}{2} \left( 1 \pm \sqrt{1 + 4a^2 + 4\Omega} \right) = \frac{1}{2} (1 \pm \Psi) \end{aligned}$$

with  $\Psi := \sqrt{1 + 4a^2 + 4\Omega}$ .

To display the solutions I introduce the generalized hypergeometric function [37] for

$p, q \in \mathbb{N}, a_i, b_j, Z \in \mathbb{R}$

$${}_pF_q(\{a_1, \dots, a_p\}, \{b_1, \dots, b_q\}, Z) = \sum_{n=0}^{\infty} \left[ \frac{\prod_{i=1}^p \prod_{k=0}^{n-1} (a_i - k)}{\prod_{i=1}^q \prod_{k=0}^{n-1} (b_i - k)} \frac{Z^n}{n!} \right].$$

For eigenvalues  $c_{0/1} = 1 \pm a$  and  $c_{2/3} = \frac{1}{2}(1 \pm \Psi)$  I obtain four solutions for  $F_{0,\dots,3}(Z)$

$$F_i(Z) = \left(-Ra a^2 e^Z\right)^{c_i} H_i(Z) \quad \text{for } i \in \{1 \dots 4\} \quad (3.11)$$

using

$$\begin{aligned} H_{0/1}(Z) &= {}_0F_3\left(\{\}, \left\{2c_{0/1} - 1, c_{0/1} + \frac{1}{2}(1 - \Psi), c_{0/1} + \frac{1}{2}(1 + \Psi)\right\}, -a^2 Ra e^Z\right), \\ H_{2/3}(Z) &= {}_0F_3\left(\{\}, \{2c_{2/3}, c_{2/3} + a, c_{2/3} - a\}, -a^2 Ra e^Z\right). \end{aligned}$$

Since I know that  $F(Z)$  has to decay faster than  $e^Z$  for  $Z \rightarrow -\infty$  using condition (3.6) and  $H_i(Z)$  is an infinite sum of terms which are either constant ( $n = 0$ ) or decaying for  $Z \rightarrow \infty$ . Hence, I only consider the two eigenvalues which are larger than 1 for the linear stability analogous because  $F_i(Z) \propto e^{Z c_i}$ . Since  $a > 0$  as well as  $\Omega \geq 0$  and hence  $\Psi \geq \frac{1}{2} + a$  we know that  $c_2 = \frac{1}{2}(1 + \Psi) > 1$ ,  $c_0 = 1 + a > 1$  and  $c_1, c_3 < 1$ .

Superposing the two solutions for  $c_0$  and  $c_2$ , the two top boundary conditions can be satisfied with non-zero constants given by  $F(0) = 0$  and  $G(0) = 0$  using (3.9) for condition I and (3.10) for condition II. Hence, I have  $F(0) = C_0 F_0(0) + C_2 F_2(0) = 0$  and an analogous equations for  $G(0)$  with  $C_0, C_2 \in \mathbb{R}$  and therefore

$$\begin{aligned} C_2 [F_0(0) G_2(0) - F_2(0) G_0(0)] &= 0, \\ C_0 [F_0(0) G_2(0) - F_2(0) G_0(0)] &= 0. \end{aligned}$$

Based on these equations we know that either  $C_0 = C_2 = 0$  or the determinant

$$\Delta(Z)|_{Z=0} = \begin{vmatrix} F_0(Z) & F_2(Z) \\ G_0(Z) & G_2(Z) \end{vmatrix}_{Z=0} = F_0(0) G_2(0) - F_2(0) G_0(0) = 0.$$

Since only the non-zero solution is physically relevant I am applying this relation at the top boundary to get a relation between the Rayleigh number  $Ra$ , the horizontal wave-number  $a$  and the non-dimensional growth rate  $\Omega$ . Based on the solutions  $F_0(Z)$  and

$F_2(Z)$  in (3.11) I can compute  $\Delta(0)$  and use the tool FindRoot for fixed values of  $a$  and  $\Omega$  to find the smallest  $Ra > 0$  satisfying the boundary condition. Based on this I compute the desired relations in the following section. This allows me to reproduce the analytical results from Wooding [14] and to extend the linear stability analysis on non-zero growth rates  $\Omega > 0$  as well as a different boundary condition (II).

### 3.3. Results

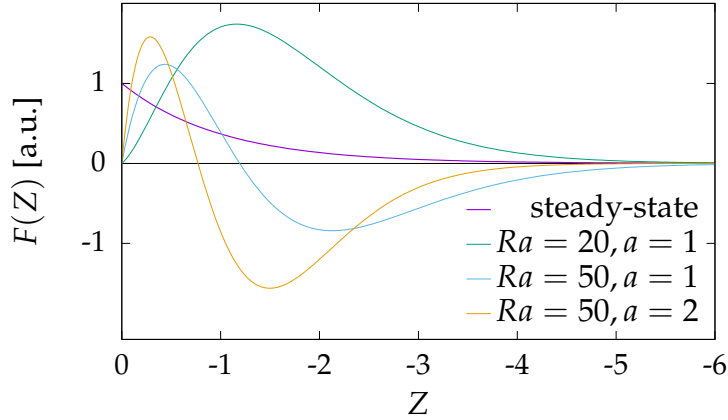


**Figure 8:** The most unstable perturbation of the vertical salinity perturbation  $F(Z)$  for exemplary wavenumber  $a$  and Rayleigh numbers  $Ra$  for  $\Omega = 0$  and  $F(Z = 0) = 0$  as well as the steady-state solution  $S^0(Z)$ . The amplitude of the functions is chosen arbitrary since the solution  $F(Z)$  can be scaled arbitrary.

In figure 8 I display exemplary solutions of the function  $F(Z)$  for different wave-numbers  $a$  and Rayleigh numbers  $Ra$ .

In figure 9 I display the neutral stability curve and the critical points for both types of boundary conditions at the surface (either constant pressure  $P$  or uniform vertical velocity  $U_Z$  corresponding to a uniform evaporation rate  $E(X, Y, \tau) = E_0$ ). I calculated the relation between the Rayleigh number  $Ra$  and the wavenumber  $a$  for a growth rate  $\Omega = 0$ . The critical points respectively the lowest points of the neutral stability curves are given in table 1.  $Ra_c$  is the smallest Rayleigh number for which the system becomes unstable.

Boundary condition	$Ra_c$	$a_c$
constant pressure	6.954	0.429
uniform flow rate	14.35	0.7585

**Table 1:** Critical wavenumber  $a_c$  and Rayleigh number  $Ra_c$ .

The numerical values of the neutral stability curve with constant pressure are equal to the results of Wooding in [14]. The critical point as well as the neutral stability curve is

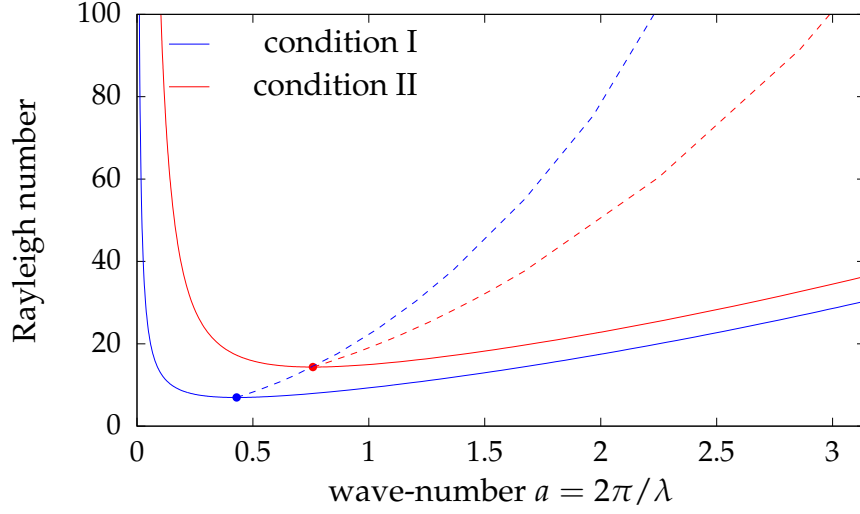


**Figure 9:** neutral stability curve  $Ra(a)$ , critical points  $Ra_c$ ,  $a_c$  and the most unstable mode according to the linear stability analysis with constant salinity at the top and either constant pressure  $P$  (I) or uniform vertical velocity  $U_Z = 1$  (II). The continuous lines represent the neutral stability curves, the dots mark the critical points and the dashed lines the most unstable mode.

equivalent with the results of Homsy and van Duijn who solved the same problem using a different approach [15, 16].

In case of uniform flow rate the critical values are larger and the system is stable in a greater regime of parameters  $Ra$  and  $a$ . Furthermore, the critical Rayleigh number is in the same order of magnitude as in the classical Elder problem analyzing the stability of a finite system with constant top and bottom boundary conditions:  $Ra_c = 4\pi^2 \approx 39.5$ . [38] Next up I compute the relation between the Rayleigh number and wavenumber for different values of the non-dimensional growth rate  $\Omega$ . In figure 10 I display the growth rate of perturbations as a function of characteristic wavenumber for different Rayleigh numbers of the system with uniform vertical velocity  $U_Z$  (condition II) at the surface  $Z = 0$ .

By computing the minima of  $a(Ra)$  for different growth rates  $\Omega$  I calculate the wavenumber with the largest growth rate  $\Omega$  as a function of the Rayleigh number  $Ra$ . This is shown in figure 11 for both types (I and II) of boundary conditions. These results point out the most unstable mode for a specific Rayleigh number. In case of random perturbation I would expect that wavenumbers near that value will dominate after in early time as long as the amplitudes are small enough. The most unstable wavenumber increases sublinear (and thereby the wavelength decreases) with increasing Rayleigh number. This resulting curve is expanding the work from Wooding, Homsy and van Duijn [14–16].

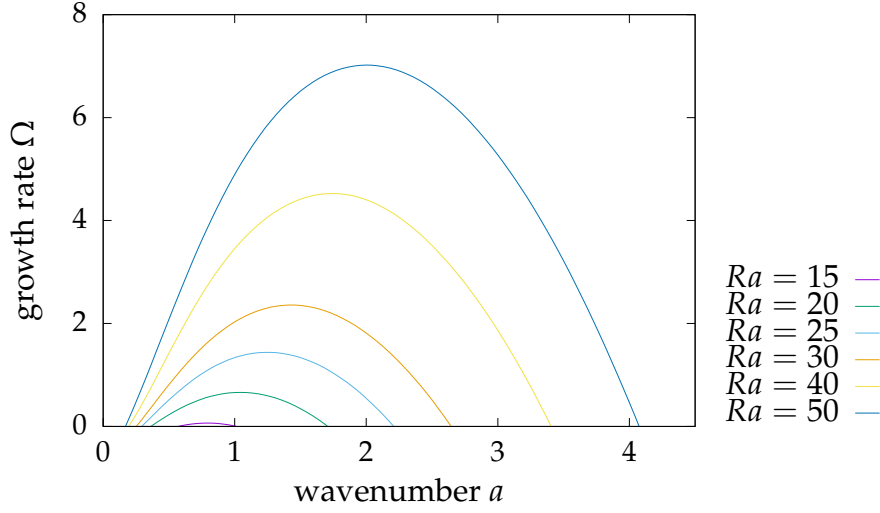


**Figure 10:** Analytical growth rates  $\Omega$  as a function of the wavenumber  $a - a_c$  (adjusted for critical wavenumber) for different Rayleigh numbers  $Ra$  for top boundary condition II corresponding uniform vertical velocity  $U_Z$ . For a condition I – constant pressure – the behavior is similar.

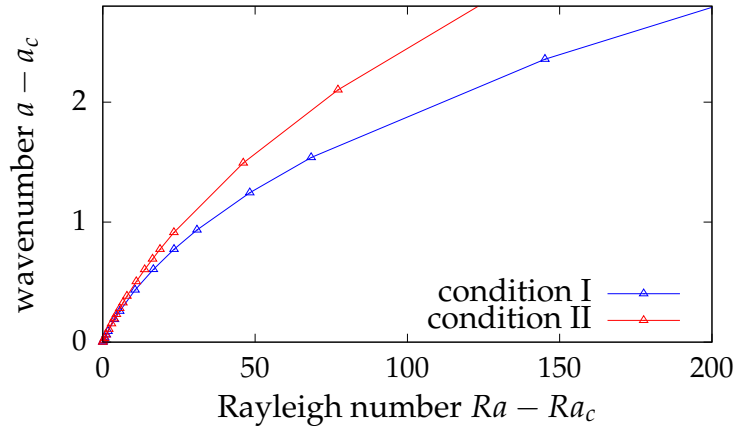


**Figure 11:** Most unstable wavenumber  $a$  as a function of the Rayleigh number  $Ra$  relative to the critical point  $Ra_c, a_c$ .



## 4. Experiments in Hele-Shaw Cells

### 4.1. Experimental methodology

Jana Lasser is performing experimental work in quasi two-dimensional Hele-Shaw cells. She aims to analyze the onset of a fingering instability and the subsequent convection rolls driven by salt concentration gradients, as well as the spacing and position of these convection rolls. Experiments are used to validate the two-dimensional numerical simulations by comparing specific measures such as the wavelength of convection cells as well as their propagation speed. The experiments constitute a simplified two-dimensional model of the real-world system of salt playa, in a controlled environment. The purpose is to investigate the convection behavior of the system for varying parameters, e.g. the evaporation rate  $E$  and Rayleigh number  $Ra$ .

In figure 12a I display the basic setup of the experiments: Two transparent plates of acrylic glass separated by a gap of size 8 mm, filled with sand. The width of the system is given by  $L = 40$  cm. At the bottom of the cell is a layer of about 5 cm sand with larger particle size (about 500 – 1000  $\mu\text{m}$ ) and thereby much larger permeability and larger Rayleigh number. On top of this layer is sand ( $H = 15$  cm) with a specified particle size of 100 – 200  $\mu\text{m}$  and a permeability of  $\kappa \approx (1.67 \pm 0.12) \times 10^{-11} \text{ m}^2$  (measured by Birte Thiede [39]). The porosity of the sand is  $\varphi \approx 0.40 \pm 0.01$  [39].<sup>1</sup>

The bottom layer with larger Rayleigh numbers aims to minimize the influence of the position of the saline water supply, which is realized by a water reservoir connected to the system via four inlets. The water level of the reservoirs is approximately 2 cm below the top of the experiment. Since there is no additional pumping, water enters the system only via the hydraulic pressure.

Due to the small gap size of the Hele-Shaw cells we assume that the flow dynamics in  $z$ -direction can be integrated and thereby neglected for the investigation [40, 41]. This setup is similar to many experiments that investigated porous media flow under controlled conditions [13, 27]. Jana Lasser combines the widely used Hele-Shaw cell setup with a new method to visualize the flow in the porous medium, as shown in figure 12b.

At the beginning the system is filled with saline water with the background concentration  $c_b = \frac{25 \text{ g salt}}{1 \text{ kg water}}$  and thereby we have a density of  $\rho_b \approx 1.016 \text{ kg/m}^3$  (using equation (2.8)). At the surface the water evaporates driving, the primary up-flow, while fresh water

<sup>1</sup>Utilizing the Carman-Kozeny equation (2.6) we can estimate the permeability of the sand with the larger particle size of about 500 – 1000  $\mu\text{m}$  in the bottom layer as  $\kappa_{\text{bottom}} \approx \kappa \left( \frac{500-1000 \mu\text{m}}{100-200 \mu\text{m}} \right)^2 \approx (42 \pm 3) \times 10^{-11} \text{ m}^2$ .

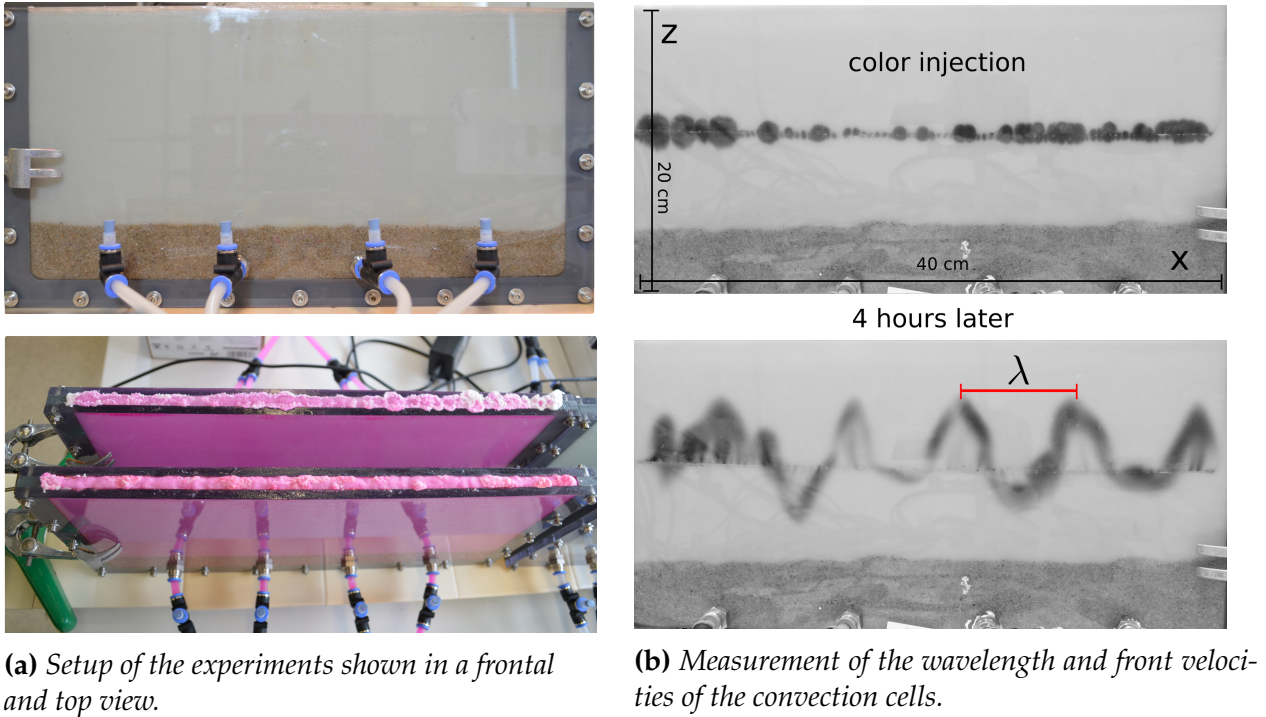


**Figure 12:** Setup of the experiments in a quasi two-dimensional Hele-Shaw cell by Jana Lasser. The interval between two transparent plates is filled with sand and salty water which is evaporating at the surface. By injecting color in a thin line the convection can be visualized.

with concentration  $c_b$  enters the system through the inlets near the bottom. The evaporation rate  $E$  can be increased by blowing away the evaporated vapor with a fan or by heating top of the experiment. The water level of the reservoir is regularly observed with a camera, to monitor the dropping water level to compute the evaporation rate. Once the water close to the surface reaches saturation, after the transient time  $\tau_s$ , salt will start to precipitate at the surface. Daily photos of the surface are taken to determine the first emergence of a salt crust.

Figure 12b shows a visualization of the flows in the cell by injection of color into the system at half height through a thin rod with small holes. Since the rod has a diameter of 1.2 mm we assume that it does not affect the flow dynamics significantly. Jana used different colors: blue, red and fluorescent. The densities of the colored water is larger than the surrounding. By regularly taking photos from the side, for a few hours, we can analyze the dynamics of the flow by tracing deformations of the line of color, and can compute the velocities of the up- and down-welling as well as the wavelengths of the occurring convection cells. These measures are established and for instance utilized by Simmons [27].

In addition, the sand can be removed irreversibly from the system layer by layer to ana-

lyze the salt concentration as a function of the horizontal and vertical position after stopping the driving of the flow. This is done to analyze the salinity distribution within convection cells for one specific point in time.

## 4.2. Experimental Results

In the following I present the experimental results from Jana Lasser which are later compared to the numerical simulation. The method to visualize the flow of the saline water in the cell is shown in figure 12b. Jana Lasser is able to measure the wavelength and the front velocities of the occurring convection cells at half height as a function of the mean evaporation rate  $E_0$  describing the vertical advective velocity in the porous medium.

By monitoring the water level in the reservoir over time Jana measures its dropping per time  $v_{\text{drop}}$ . To calculate the evaporation rate I have to adjust the height of the dropped water level with the ratio of the reservoir area over the surface area of the Hele-Shaw cell. The latter is about  $0.8 \text{ cm} \times 40 \text{ cm} \approx 32 \text{ cm}^2$  and the ratio approximately  $\sigma_{\text{area}} = 15$ . Since the dropping water level corresponds to the superficial velocity  $\mathbf{q} = \varphi \mathbf{v}$  we have  $E_0 = \frac{v_{\text{drop}} \sigma_{\text{area}}}{\varphi}$ . The mass flow rate through the surface then is  $\varphi E_0$ .

For each experiment we take the images of the water level in the time period of 24 hours before and after the coloring itself to compute the respective evaporation rate by linear least-square fitting the water level. The coloring experiment itself have durations of about 4 hours – the time interval for determining the velocities. Based on this we get values for the evaporation rate ranging from about 2 to 4  $\mu\text{m/s}$ . Some experiments do not have valid evaporation measurements since the monitoring did not work properly. Since we only have rough estimations they will be neglected for our comparison with the numerical simulation.

In case that there is a salt crust on the surface while doing the coloring experiment it can be assumed that the saturation at the surface is already reached. Since for some of the experiments there is no crust on the surface at the time of the coloring so that we need to estimate the density at the surface to compute the density difference  $\Delta\rho$  and the Rayleigh number  $Ra \propto \Delta\rho$ . For that purpose we utilize the analytical solution of the transient in section 2.6. In dimensionless time (with  $T = D/E_0^2$ ) we have a dimensionless saturation time  $\tau_s = 13.2$  for a background salt concentration of 2.5% used in the experiment.

Taylor estimated the velocity-dependent dispersion  $D_U$  in [42] by

$$D_U = D \left( \frac{U^2 r_{\text{particles}}^2}{48 D_M^2} \right) \approx 0.03D \ll D \quad (4.1)$$

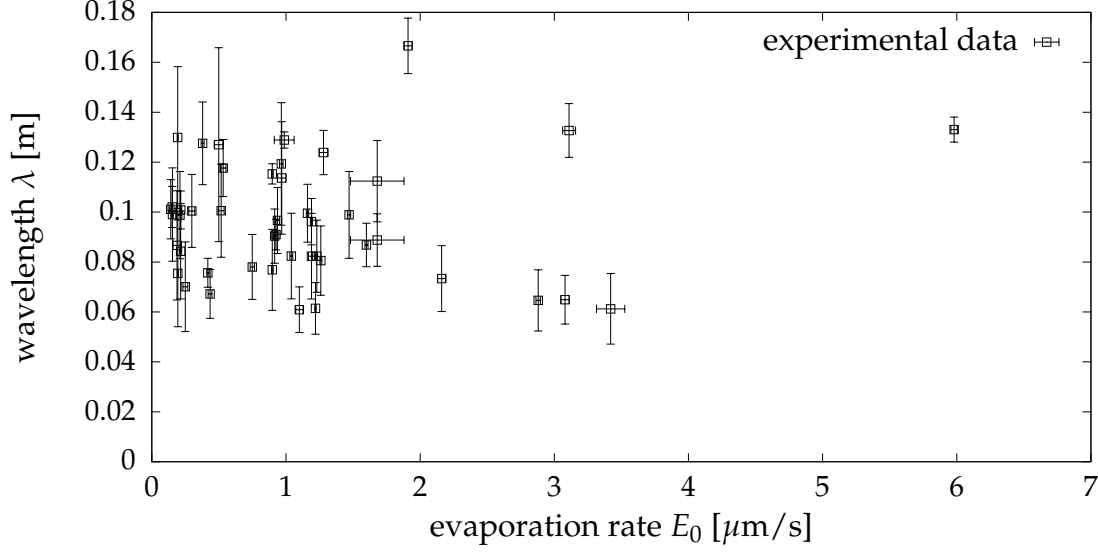


**Figure 13:** Wavelength  $\lambda$  of convection cells as a function of the evaporation rate  $E_0$  of the experiment.

with molecular diffusion for sodium chloride in water  $D = 0.805 \times 10^{-9} \text{ m}^2/\text{s}$  at  $25^\circ\text{C}$  [43], the particle radius  $r_{\text{particles}} \approx 200 \text{ }\mu\text{m}$  the characteristic front velocity  $U \approx 5 \text{ }\mu\text{m/s}$ . Hence, the molecular diffusion dominates and I will not consider the velocity-dependent dispersion.

Now, I compute the saturation time using the diffusion  $D = 0.805 \times 10^{-9} \text{ m}^2/\text{s}$ . If the coloring experiments take place later than  $2t_s$  I assume that saturation at the surface is already reached and we have the maximal density difference  $\Delta\rho$ . The other coloring experiments will not be considered for the validation of the numerical simulations since the numerical model considers constant salt concentration at the top boundary. Now, 46 coloring experiments with either an emerged salt crust or  $t > 2t_s$  remain. In the latter cases the crust emerged in the following one or two days.

Using the side-view images of the cell (compare figure 12b) during the coloring Jana Lasser quantified the wavelengths of the occurring convection rolls by measuring the distance of the maxima respective minima. This gives values between 5 and 12 cm. In figure 13 I show the measured wavelengths for each experiment as a function of the evaporation rate  $E_0$ . Here, no clear trend is visible. The increased density of the saline water with the color will not have any direct effect on the wavelength.

Given her monitored images and tracking the fastest up- and downwelling fronts of the occurring convection rolls Jana also measures the maximal front velocity. Over a time period of several hours the fronts typically move a few millimeters. Analyzing the spatial shift of the colored line at half height we thus have a proxy for the velocity at half height, since we assume that the front velocity does not vary significantly over a few millimeters.

The typical front velocities ranges from  $1.5 - 11 \mu\text{m/s}$ .

We have measurements of 16 coloring experiments with different colors, mostly blue. Since the density of the colored salt water is slightly larger I expect a relative downwelling trend of the velocities although it is not obvious whether this is dominating the overall upwelling due to the evaporation. The mean value of the maximal up- and downwelling front velocities as a function of the evaporation rate is shown in figure 14. The value should not be influenced of the density of the colored water since the larger density will lead to a constant downwelling of the complete color line. Figure 15 shows the difference of these values:  $v_{\text{up}} - v_{\text{down}}$  for the maximal front velocities. The downwelling front velocity is larger in most of the experiments. Although we have an overall upstream the increased density and enhanced downwelling of the color front relative to the convection itself may explain this.

Based on these measurements I check whether turbulence is of relevance for our problem. For that purpose I estimate the Reynold number for flow in porous media based on the work of Ergun [44, 45]. Using the particle radius  $r_{\text{particle}} \approx 200 \mu\text{m}$ , the density of water  $\rho = 1 \times 10^3 \text{ kg/m}^3$ , the characteristic front velocity  $U \approx 5 \times 10^{-6} \text{ m/s}$ , the porosity  $\varphi \approx 0.4$  and the viscosity  $\mu_0 = 1 \times 10^{-3} \text{ kg/(ms)}$  we have

$$Re = \frac{\rho a_{\text{particle}} U}{\mu_0 (1 - \varphi)} \approx 2 \cdot 10^{-3} \ll 1.$$

Since Ergun [44] observed a critical value of  $3 - 10$  it can be safely assumed that there is no turbulence occurring in the experiments.

Later I will compare these results with the numerical simulation in order to check consistency of the order of magnitude of the wavelength and the velocities as well as its dependency of the Rayleigh number.

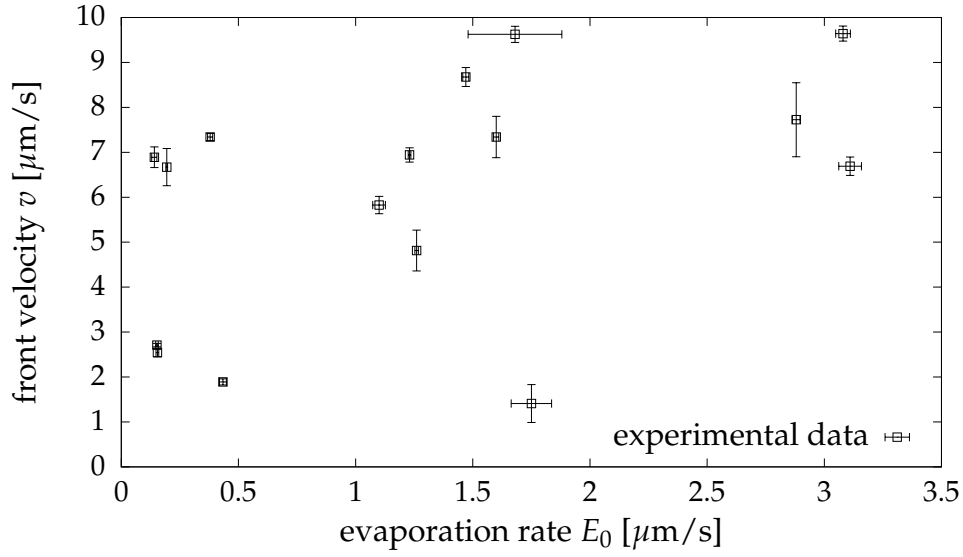


**Figure 14:** Mean of the maximal up- and downwelling front speed  $\frac{v_{up} + v_{down}}{2}$  as a function of the evaporation rate  $E_0$ .

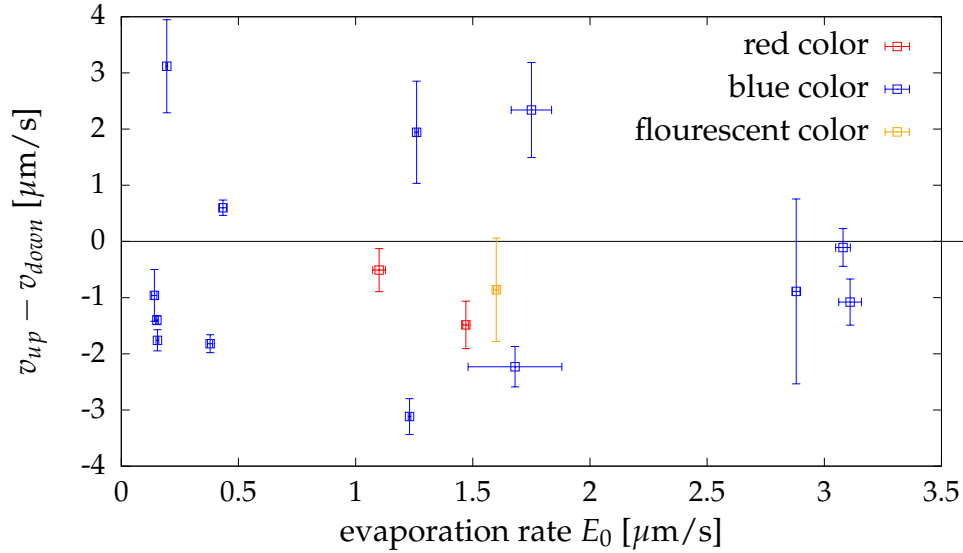


**Figure 15:** Difference of the maximal up- and downwelling front velocity  $v_{up} - v_{down}$  as a function of the evaporation rate  $E_0$ . The downwelling velocity is larger in most coloring experiments (blue, red and fluorescent).

## 5. Double-periodic simulations

Before implementing the two-dimensional numerical model of convection in salt playa I will reproduce the numerical work done by Rogerson and Meiburg in 1993 [17] in this chapter. They accomplished two-dimensional, double-periodic numerical simulations of the evolution of the interface for two miscible fluids with differing densities and viscosities in a porous medium under gravitational influence.

Considering the similarities of the approaches I reproduce their numerical work as a preparatory work to the actual implementation of the numerical model of the salt playa convection since it helps to validate the simpler spectral approach before applying pseudo-spectral approaches to solve the Poisson equation in section 6 for our model of convection in salt playa.

The dynamical behavior of the system, as well as the differential equations, are quite similar to the system described in chapter 2 as well as the utilized methods. The main difference is that I have non-periodic boundary conditions in the  $y$ -direction in that system while Rogerson utilizes periodic boundary conditions in both  $x$ - and  $y$ -direction. He uses a spectral approach to solve the differential equations by transforming the differential equations to Fourier space, solve them and transform it back.

### 5.1. Implementation

Given is a two-dimensional system of size  $L \times H$  in  $x$ - and  $y$ -direction. The length and height are given by  $L$  and  $H$ . I introduce the dimensionless Peclet number  $Pe := H$  and the aspect ratio  $A := L/H$  so that  $L = Pe A$ . Unlike Rogerson, who considers an angle  $\theta$  of the gravitation relative to  $\hat{\mathbf{z}}$ , I assume that  $\mathbf{g} \parallel \hat{\mathbf{z}}$  since I only consider the case  $\theta = \pi/2$  (compare [17]).

In figure 16 I display the basic flow configuration of the system: We have an overall flow of  $U = 1$  in the  $x$ -direction (dimensionless) and an initial interface between the two fluids is parallel to the  $y$ -axis. The fluids themselves have velocities of  $V_1$  and  $V_2$  in  $y$ -direction which is tangential to their initial interface. The distribution of the two fluids is described by the concentration field  $c(x,y)$  with  $c = 1$  for the first fluid and  $c = 0$  for the second fluid. The density and viscosity is concentration dependent and given by  $\mu(c) = e^{R(1-c)}$  and  $\rho(c) = e^{S(1-c)}$  with dimensionless parameters  $R$  and  $S$ .

Analogous to Rogerson and Meiburg in [17] I consider a reference frame moving with  $U = 1$  in  $x$ -direction and average tangential velocity  $V_0 = \frac{1}{2}(V_1 + V_2)$  in the  $y$ -direction

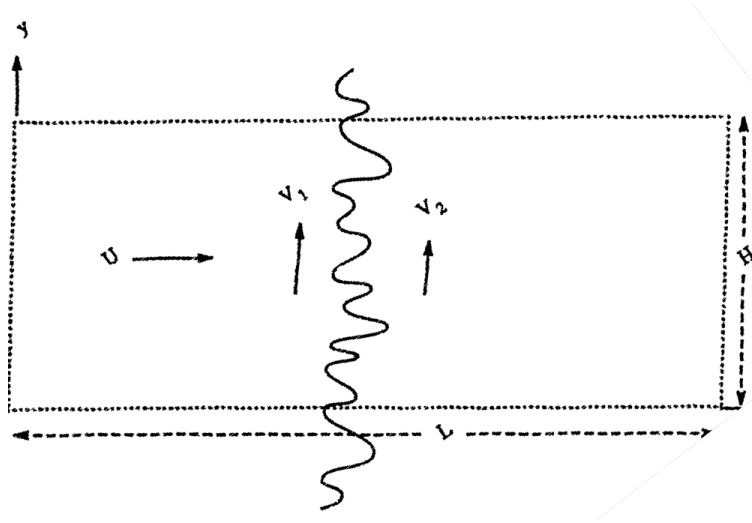


**Figure 16:** Sketch of the flow configuration in the numerical simulations done by Rogerson and Meiburg [17]. We have a concentration field ranging from  $c = 1$  (left) to  $c = 0$  (right). We have  $L = Pe A$  and  $H = Pe$  and gravitation directed in  $z$ -direction. Sketch adapted from [17].

and use the equations neglecting the dependency on  $\theta$ :

$$\nabla \cdot \mathbf{U} = 0, \quad (5.1)$$

$$\nabla P = -\mu \mathbf{U} + G \rho \hat{\mathbf{x}}, \quad (5.2)$$

$$\frac{\partial c}{\partial \tau} + \mathbf{U} \cdot \nabla c = \nabla^2 c. \quad (5.3)$$

The dimensionless parameter  $G$  corresponds to the ratio of the gravitational to the viscous forces. In the left boundary I have the fluid 1 and at the right boundary fluid 2 with their respective velocities. Hence, the boundary conditions in the  $x$ -direction are given by  $c = 1$ ,  $\mathbf{U} = (0, V_1 - V_0)$  at  $x = 0$  and  $c = 0$ ,  $\mathbf{U} = (0, V_2 - V_0)$  at  $x = L = Pe A$ . In  $y$ -direction I assume periodicity and thereby have  $\mathbf{U}(x, 0) = \mathbf{U}(x, H)$ .

For numerical analysis I use a stream function-vorticity formulation following Rogerson and Meiburg [17]. For a two-dimensional and incompressible flow we can define the Laplace stream function [18, 41, 46]  $\psi(x, y, \tau)$  fulfilling the condition  $\mathbf{U} = (\frac{\partial \psi}{\partial y}, -\frac{\partial \psi}{\partial x})$ . It follows that the incompressibility is fulfilled by definition:  $\nabla \cdot \mathbf{U} = 0$ . Instead we use the vorticity  $\omega = (\nabla \times \mathbf{U})_z$  which fulfills the Poisson equation  $\nabla^2 \psi = -\omega$ . This approach allows one to simplify equation (5.2) by eliminating the pressure dependency. As shown



by Rogerson and Meiburg [17] the equations become

$$\begin{aligned}\nabla^2 \psi &= -\omega \\ \omega &= -R [(\psi_x - V_0) c_x + (\psi_y + 1) c_y] + G S e^{(S-R)(1-c)} c_y, \\ c_\tau &= -\psi_y c_x + \psi_x c_y + c_{xx} + c_{yy},\end{aligned}$$

with the derivatives of  $c$  and  $\psi$  in the  $x$ ,  $y$ -directions as well as time  $\tau$ . We now aim to solve the Poisson equation using a purely spectral method.

I introduce a periodic extension in  $x$ -direction by reflecting the two-dimensional system of size at  $x = L$  and compute the differential equations in the double-size system with a length of  $2L$ . Now there are two interfaces and I can assume periodicity in both directions and utilize a spectral method to solve the Poisson equation.

The numerical methods are outlined in [17, 47]. The second interface of the two fluids which is at  $x = 3L/2$  is stable for  $R > 0$  since the viscosity of the second fluid is larger. We stop simulating before the developing fingers reach the second interface. I utilize the Fourier expansions with wavenumbers  $k_m = \frac{2\pi m}{Pe A}$  and  $k_n = \frac{2\pi n}{Pe}$  ( $m, n \in \mathbb{Z}$ ), for the concentration field  $c(x, y, \tau)$

$$c(x, y, \tau) = \sum_{m=-M/2}^{M/2-1} \sum_{n=-N/2}^{N/2-1} \hat{c}_{m,n}(\tau) e^{i(k_m x + k_n y)} \quad (5.4)$$

and analogous for  $\psi$  and  $\omega$ . I use the  $M \times N$  grid points:  $x_j = j \frac{Pe A}{M}$  and  $y_l = l \frac{Pe}{N}$  for  $j, l \in \mathbb{N}^0$  and  $j \leq M-1$ ,  $l \leq N-1$  and introduce the functions  $J, K$  and  $L$

$$\begin{aligned}J(x, y, \tau) &= \psi_y c_x - \psi_x c_y, \\ K(x, y, \tau) &= G S e^{(S-R)(1-c)} c_y, \\ L(x, y, \tau) &= \psi_x c_x + \psi_y c_y\end{aligned} \quad (5.5)$$

and their respective Fourier transformation. These functions represent the non-linear terms in the differential equations and are computed in real space. Since the differential equations are computed in Fourier space they have to be Fourier transformed. The equations of the vorticity, stream function and concentration fields, using  $J, K$  and  $L$ , in Fourier

space are:

$$\begin{aligned}\hat{\omega}_{m,n} &= -R \left( \hat{L}_{m,n} + i (k_n - k_m V_0) \hat{c}_{m,n} \right) + \hat{K}_{m,n}, \\ \hat{\psi}_{m,n} &= \frac{\hat{\omega}_{m,n}}{k_m^2 + k_n^2}, \\ \frac{\partial \hat{c}_{m,n}}{\partial \tau} &= -\hat{J}_{m,n} - (k_m^2 + k_n^2) \hat{c}_{m,n}.\end{aligned}$$

These equations are solved in Fourier space and the results transformed back into real space to compute the derivatives of  $\psi$  and  $c$  and the nonlinear terms  $J, K$  and  $L$  with a standard central finite difference scheme of second-order. Then these fields are transformed back into Fourier space for the next step. For computing the Fourier transformation in each integration step I use a FFT algorithm.

The time-stepping is done by using a second-order, linear multi step Adams-Bashforth method [47]. I use adaptive time steps utilizing the Courant–Friedrichs–Lewy condition  $C = \frac{u_{\max} \Delta \tau}{\Delta x} \leq C_0$  [48] with a constant  $C_0 = \mathcal{O}(1)$  which is chosen as 0.1 to reach stability. I compute the maximal velocity every tenth step and adjust  $\Delta \tau$  so that  $C = C_0 = 0.1$ .

## 5.2. Validation

In the following I will present some examples of qualitative and quantitative results and compare them to the work of Rogerson and Meiburg [17] in order to validate my implementation of the simulation. For that purpose I consider the behavior of small concentration perturbations near the interface of the two fluids using the quantitative measures of the growth rate  $\Omega$  of the amplitude  $A_\Omega$  with  $A_\Omega(\tau) \propto e^{\Omega \tau}$ . In addition to this I consider the wavelength of fingers for early times. These measures are relevant to validate the simulation of such systems for small deviations from the steady-state and will later be used to validate the simulation of the salt playa convection patterns. In figure 17 I display several snapshots of the relative concentration of fluid for a system with neither buoyancy ( $S = 0$ ) nor tangential velocities ( $V_1 = V_2 = 0$ ). The instabilities are driven by the viscosity contrast. The qualitative behavior of the development of the occurring fingering structure is similar to that found by Rogerson and Meiburg, e.g. the coarsening behavior [17].

Tan and Homsy performed a linear stability analysis for such a system [49] and computed the characteristic wavelength of the occurring fingers at a given time. For the system with  $H = Pe = 1000$ ,  $R = 3$ ,  $G = S = 0$  at time  $\tau = 100$  I get an average wavelength of the fingers of  $\lambda = Pe/N_{\text{finger}} \approx 60.6 \pm 0.8$  (standard error when running the simulation 20 times). In the simulations I use white noise as initial condition of the concentration

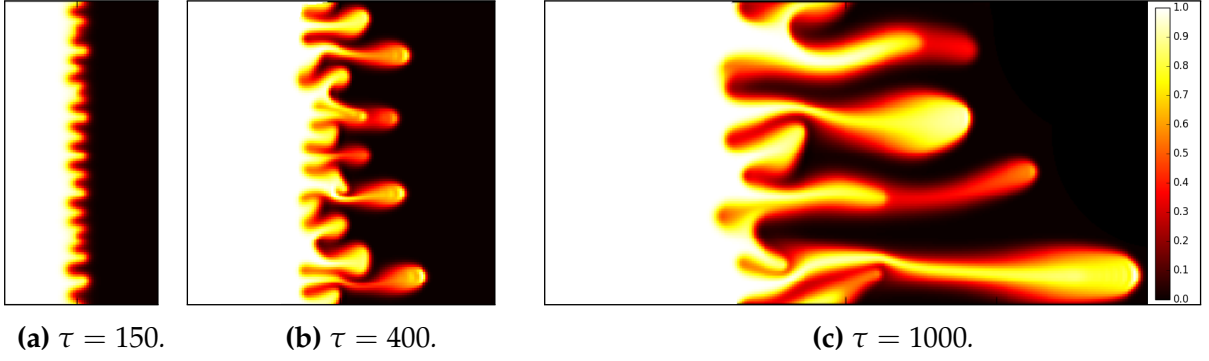


**Figure 17:** Concentration  $c$  (from  $c = 0$  (black) to  $c = 1$  (white)) and for a system with  $Pe = 1000$ ,  $R = 3$ ,  $G = S = 0$ ,  $V_1 = V_2 = 0$ ,  $A = 2$  for some exemplary time frames. We can clearly see the fingering pattern in the horizontal direction.

near the interface with an amplitude 0.01. This result is consistent with the theoretically predicted  $\lambda \approx 61.3$  as well as the numerical result of Rogerson and Meiburg  $\lambda \approx 58.8$  [17] who performed this validation just once.

Next I compare the growth rates of small concentration perturbations in a system with buoyancy ( $S > 0$ ) and non-zero tangential velocities of the fluids. According to Rogerson I utilize the following periodic concentration perturbation with amplitude  $\gamma = 10^{-3}$  in  $y$ -direction, with wavenumber  $a = 2\pi/Pe$ :

$$\tilde{c}(x, y, t_0) = -\gamma \cos(ay) \exp\left(-\frac{(x - x_{\text{interface}})^2}{4}\right).$$

The cosine-term represents the separated function of the perturbation in  $y$ -direction and the exponential term the width of the perturbation in  $x$ -direction.

Following Rogerson and Meiburg I compute the root mean square (rms) of the deviation of the concentration at each time in the area of size  $L \times H$  relative to the concentration at that time for the evolved system without perturbation. This gives the amplitude and the logarithmic growth rates  $\Omega$  (with  $A_\Omega(\tau) \propto e^{\Omega\tau}$ ). I compute the same for the  $U$ -velocity in  $x$ -direction. Furthermore, I compute the growth rates of the velocity perturbation for constant time as a function of the wavenumber  $a$ . The comparison of my own results and the results of Rogerson and Meiburg in [17] are shown in figure 18 (time-dependence) and 19 (wavenumber-dependence). The curves in both figures show very good agreement.

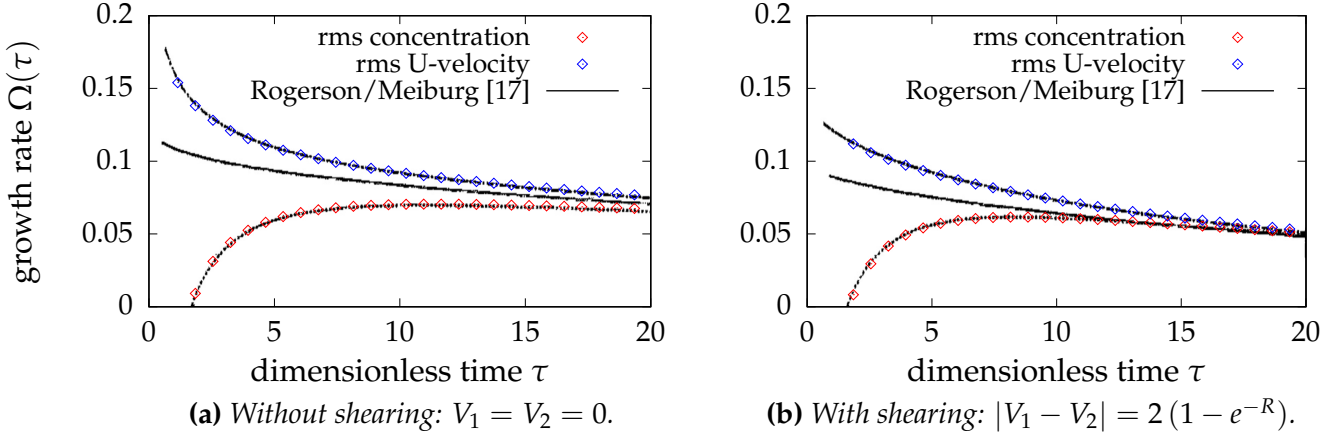


**Figure 18:** Shown are the dimensionless growth rates,  $\Omega(\tau)$  as a function of time for a system with  $R = 3$ ,  $S = -2$ ,  $G = 1$  and wavenumber  $a = 0.15$ . The black lines correspond to the results of Rogerson and Meiburg in [17] whereby the central curve is the results from the theoretical linear stability analysis. The upper curve is the numerical growth rate of the root mean square of a small concentration perturbation and the bottom curve for the U-velocity in x-direction. The colored points represent results from my simulation.

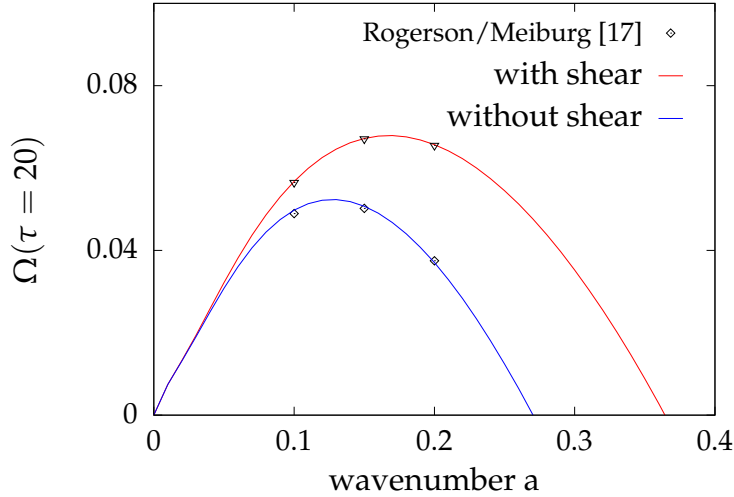


**Figure 19:** Shown are the growth rates  $\Omega(a)$  of the velocity perturbation at dimensionless time  $\tau = 20$  as a function of wavenumber  $k$  for the same parameters as in figure 18. The black dots corresponds to the results of Rogerson in [17] and the colored curves are results from my simulation: blue corresponds to shearing  $|V_1 - V_2| = 2(1 - e^{-R})$  and red to the case without shear  $V_1 = V_2 = 0$ .

## 6. Implementation of the model

In the previous chapter 5 I reproduced the numerical work of Rogerson and Meiburg [17]. In the following I present the methods used to implement a two-dimensional, finite-difference model of the salt playa based on the non-dimensional equations given in (2.10), (2.11) and (2.12). I have a two-dimensional system with height  $H$  in the  $Z$ -direction and length  $L$  in the  $X$ -direction and assume periodicity in the latter direction. I model the system with saturation at the top boundary,  $\rho(Z = 0) = \rho_s$ , and thereby  $S(Z = 0) = 1$  for  $\rho_m = \rho_s$  using the definition of non-dimensional salinity (2.9).

Additionally I have background concentration at the bottom boundary  $\rho(Z = -H) = \rho_b$  and hence  $S(Z = -H) = 0$ .

Within the scope of my thesis I neglect the effect of varying viscosity and use  $\mu(S) = \mu(0)$ . Wooding argues that this assumption only alters the results to a minor degree [13]. Further, I only account for molecular diffusion expressed with a scalar diffusion coefficient  $D$  and do not consider any velocity or concentration dependent diffusion and dispersion. Notwithstanding the known importance of velocity-induced dispersion in porous media [42] many authors in the field, such as the references [17, 19, 20, 47] in like manner assume a scalar diffusion constant. I follow [19, 20] in accounting for a scalar diffusion constant only. In the experimental chapter 4 I showed that the velocity-dependent dispersion is small relative to the molecular diffusion and thereby can be safely neglected for our simulation.

At the surface of the system ( $Z = 0$ ) I have an imposed evaporation rate  $E(X)$  with average  $\langle E(X) \rangle_X = E_0$  driven by external forces such as heating. This corresponds to a vertical velocity  $U_Z(X, Z = 0)$  with average  $\langle U_Z(X, Z = 0) \rangle_X = -1$ . In the first part of the investigation I use a uniform evaporation rate  $U_Z(X, Z = 0) = -1$ . In the section 7.4 I study a possible connection of the salt ridge patterns on the surface and the subsurface convection cells by imposing a sinusoidal evaporation rate and analyzing the influence of such variations.

Since I assume incompressibility we know that  $\langle U_Z(X, Z) \rangle_X = -1$  for  $Z \neq 0$ . For reasons of simplification I assume a uniform flow rate  $U_Z(X, Z = -H) = -1$  at the bottom boundary. Assuming constant pressure may be more realistic and could be investigated in subsequent work.

For the implementation I follow the numerical approach of Ruith and Meiburg [19], Riaz and Meiburg [20] as well as Chen [21] making use of a semi-spectral approach to solve the Poisson equation, compact finite difference schemes of sixth-order to compute the derivatives as well as an explicit third-order Runge-Kutta scheme for time stepping introduced

by [23].

## 6.1. Differential equations

I use the following set of non-dimensional equations for a two-dimensional and planar system

$$\begin{aligned}\nabla \cdot \mathbf{U}(X, Z, \tau) &= 0, \\ \frac{\partial S(X, Z, \tau)}{\partial \tau} &= -\mathbf{U}(X, Z, \tau) \cdot \nabla S(X, Z, \tau) + \nabla^2 S(X, Z, \tau), \\ \mathbf{U}(X, Z, \tau) &= -\nabla P(X, Z, \tau) - Ra S(X, Z, \tau) \hat{\mathbf{Z}}.\end{aligned}\tag{6.1}$$

In case of uniform evaporation rate respectively vertical velocity at the top surface I have  $U_Z(X) = -1$ . Since I investigate variations in top evaporation rate I introduce the analytical function  $U_Z^0(X)$  which is 0 in the uniform case and represents the variations in the boundary condition.

The vertical boundary conditions are the following:

top boundary $Z = 0$	bottom boundary $Z = -H$
$S(X) = 1$	$S(X) = 0$
$U_Z(X) = -1 - U_Z^0(X)$	$U_Z(X) = -1$

Analogous to the preparatory work in chapter 5, I utilize a stream function-vorticity approach following [19, 20]. The Laplace stream function  $\psi(X, Z, \tau)$  only accounts for the variations from the uniform base flow in vertical direction. The stream function  $\psi(X, Z, \tau)$  and vorticity  $\omega(X, Z, \tau)$  corresponding to the curl in the third  $Y$ -direction satisfy

$$\begin{aligned}\mathbf{U} &= \frac{\partial \psi}{\partial Z} \hat{\mathbf{X}} + \left(-1 - \frac{\partial \psi}{\partial X}\right) \hat{\mathbf{Z}}, \\ \omega &= (\nabla \times \mathbf{U})_Y.\end{aligned}$$

With this approach the incompressibility condition is still satisfied since

$$\nabla \cdot \mathbf{U} = \frac{\partial}{\partial X} \frac{\partial \psi}{\partial Z} - \frac{\partial}{\partial Z} \left(-1 - \frac{\partial \psi}{\partial X}\right) = 0.$$

The vorticity function satisfies the Poisson equation

$$\nabla^2 \psi = -\omega.\tag{6.2}$$

Taking the curl of the Darcy law I can eliminate the pressure term, since  $\nabla \times \nabla \Phi = 0$  for arbitrary scalar fields  $\Phi$ , and get

$$\begin{aligned} (\nabla \times \mathbf{U}(X, Z, \tau))_Y &= \left( -\nabla \times \nabla P(X, Z, \tau) - \nabla \times \left[ Ra S(X, Z, \tau) \hat{Z} \right] \right)_Y \\ \Rightarrow \omega(X, Z, \tau) &= \partial_X [Ra S(X, Z, \tau)] = Ra \partial_X S(X, Z, \tau). \end{aligned} \quad (6.3)$$

Based on the new formulation of differential equations (6.2), (6.1) and (6.3) we can calculate the adapted boundary conditions for the stream function  $\psi$  and the vorticity  $\omega$ . The constant vertical flow for the boundaries transforms to

$$U_Z(X, Z = 0) = -1 - U_Z^0(X) \quad \Rightarrow \quad \frac{\partial \psi(X, Z = 0)}{\partial X} = U_Z^0(X) \quad (6.4)$$

$$U_Z(X, Z = -H) = -1 \quad \Rightarrow \quad \frac{\partial \psi(X, Z = -H)}{\partial X} = 0 \quad (6.5)$$

Constant salinity in the horizontal direction corresponds to a vanishing vorticity  $\omega = 0$  using (6.3).

Following Chen in [21] I split the velocity in two components. Imposing a vertical flow rate  $U_Z(X, Z = 0) = -1 - U_Z^0(X, Z = 0)$  at the top boundary I introduce a stream function potential  $\psi^0(X, Z)$  that is constant in time satisfying (6.4) and (6.5). I now split the stream function  $\psi$ , the vorticity  $\omega$  and the velocity  $\mathbf{U}$  in two components

$$\begin{aligned} \psi(X, Z, \tau) &= \tilde{\psi}(X, Z, \tau) + \psi^0(X, Z), \\ \omega(X, Z, \tau) &= \tilde{\omega}(X, Z, \tau) + \omega^0(X, Z) = \tilde{\omega}(X, Z, \tau) + \nabla^2 \psi^0(X, Z), \\ \mathbf{U}(X, Z, \tau) &= \tilde{\mathbf{U}}(X, Z, \tau) + \mathbf{U}^0(X, Z) = \tilde{\mathbf{U}}(X, Z, \tau) + \frac{\partial \psi^0}{\partial Z} \hat{\mathbf{x}} - \frac{\partial \psi^0}{\partial X} \hat{\mathbf{z}}. \end{aligned}$$

with their respective analytical expressions for  $\psi^0(X, Z)$ ,  $\omega^0(X, Z)$  and  $\mathbf{U}^0(X, Z)$ . These analytical functions represent the constant part of the solutions and are non-zero if the evaporation rate does vary on the top boundary. Imposing a varying evaporation rate at the surface can be done by using an analytical expressions for  $\psi^0(X, Z)$ . I then solve the Poisson equation for  $\tilde{\psi}(X, Z, \tau)$  and  $\tilde{\omega}(X, Z, \tau)$ .

The top boundary condition now reads  $\tilde{\psi}(X, Z = 0) = \text{const}$  and analogous for the bottom boundary  $Z = -H$ . I can set  $\tilde{\psi}(X, Z = 0) = 0$  and then

$$\tilde{\psi}(X, Z = -H) = \int_0^{-H} \frac{\partial \tilde{\psi}(X, Z)}{\partial Z} dZ = \int_0^{-H} \tilde{U}_X(X, Z) dZ.$$

Imposing an initial condition without a uniform vertical flow and boundaries not con-

tributing horizontal momentum. Hence,  $\tilde{\psi}(X, Z = -H) = 0$  due to momentum conservation.

Collecting the modified differential equations I now have

$$\tilde{\omega}(X, Z, \tau) = Ra \partial_X S(X, Z, \tau) - \omega^0(X, Z), \quad (6.6)$$

$$\nabla^2 \tilde{\psi}(X, Z, \tau) = -\tilde{\omega}(X, Z, \tau), \quad (6.7)$$

$$\mathbf{U}(X, Z, \tau) = \left( \frac{\partial \tilde{\psi}(X, Z, \tau)}{\partial Z} + \frac{\partial \psi^0(X, Z)}{\partial Z} \right) \hat{\mathbf{x}} + \left( -1 - \frac{\partial \tilde{\psi}(X, Z, \tau)}{\partial X} - \frac{\partial \psi^0(X, Z)}{\partial X} \right) \hat{\mathbf{z}}, \quad (6.8)$$

$$\frac{\partial S(X, Z, \tau)}{\partial \tau} = -\mathbf{U}(X, Z, \tau) \cdot \nabla S(X, Z, \tau) + \nabla^2 S(X, Z, \tau). \quad (6.9)$$

with the boundary conditions satisfying

top boundary $Z = 0$	bottom boundary $Z = -H$
$S(X) = 1$	$S(X) = 0$
$\omega(X) = 0$	$\omega(X) = 0$
$\tilde{\psi}(X) = 0$	$\tilde{\psi}(X) = 0$

Using (6.9) I compute the steady-state of the salinity distribution  $S^0(X, Z)$  fulfilling the boundary conditions  $S(X, Z = 0) = 1$  and  $S(X, Z = -H) = 0$  and get

$$S^0(X, Z) = \frac{e^{-Z}}{1 - e^{-H}} - \frac{e^{-H}}{1 - e^{-H}}. \quad (6.10)$$

In the numerical simulations I typically make use of this  $S^0(X, Z)$  as initial condition. Alternatively, to study the stability of convection cells, I start with an evolved convection cell, as will be introduced in chapter 7.2.

Following Riaz and Meiburg [20] I use the random initial salinity perturbations to trigger a non-uniform dynamics by convolving a field of random numbers  $f(X, Z)$  uniformly distributed in  $[-1, 1]$ , an amplitude of  $\gamma$  and an exponential kernel with a width of  $\sigma$ , typically chosen as  $\sigma = 3$ , to avoid grid artifacts in the derivatives:

$$\tilde{S}_{\text{random}}(X, Z) = \gamma f(X, Z) * e^{-\frac{X^2 + Z^2}{\sigma^2}}. \quad (6.11)$$

The implementation details of the time-stepping, the calculation of derivatives as well as solving the Poisson equation using a semi-spectral approach are described in the following sections.



## 6.2. Compact finite difference schemes

To compute the first- and second derivatives of  $S(X,Z)$  and  $\psi(X,Z)$  in the differential equations I make use of sixth order compact finite difference schemes, an implicit method [22, 50]. In the  $X$ -direction I utilize periodic boundary conditions and in the  $Z$ -direction I have Dirichlet boundary conditions. In comparison to the standard finite difference schemes the compact finite difference schemes allows for higher order accuracy and stability. Particularly for the Dirichlet boundary conditions accuracy is of the same high order at the boundaries, which is important since since the accuracy there is crucial for the stability of a numerical simulation. The generalized approach is introduced by Lele [22] and Tyler [50]. Tyler [50] computed high order scheme for the first and second derivatives for interior as well as boundary grid points.

A standard centered finite difference schemes for a first order derivative is

$$f'_i = \frac{f_{i+1} - f_{i-1}}{2h}$$

for a function  $f$  at the discrete points  $x_i = h \cdot i$ ,  $i \in \mathbb{N}$  and  $0 \leq i \leq N - 1$ , and grid spacing  $h$ . Using a Taylor expansion of the function  $f$  around  $x_i$  one can compute the local truncation error and gets  $\mathcal{O}(h^2)$ . [50]

Lele [22] generalized the form of the compact finite difference scheme for first order derivatives for an interior grid point  $i$  at  $x_i$

$$f'_i + \sum_{j=1}^{l_\alpha} \alpha_j (f'_{i+j} + f'_{i-j}) = \sum_{j=1}^{l_a} a_j \frac{f_{i+j} - f_{i-j}}{2jh}$$

with constants  $\alpha$  and  $a$  which need to be determined depending of the stencil size  $l_\alpha$  and  $l_a$  as well as the desired order of the scheme [22].

According to [50] we have for a second derivative with stencil size  $l_\beta$  and  $l_b$

$$f''_i + \sum_{j=1}^{l_\beta} \beta_j (f''_{i+j} + f''_{i-j}) = \sum_{j=1}^{l_b} b_j \frac{f_{i+j} - f_i + f_{i-j}}{j^2 h^2}.$$

For periodic boundary conditions in  $x$ -direction these linear equations can be computed for every grid point since  $f_0 = f_L$ . In case of Dirichlet boundary conditions at the top and bottom of the system we need to utilize non-symmetric schemes such as

$$f'_0 + \sum_{j=1}^{l_\alpha} \alpha_j f'_j = \frac{1}{h} \left( \sum_{j=1}^{l_a} a_j f_j \right)$$

**Table 2:** Coefficients for sixth compact finite difference schemes used in the numerical simulations.  
Coefficients for first derivatives  $f'$ .

	$\alpha_0$	$\alpha_1$	$a_1$	$a_2$	$a_3$	$a_4$	$a_5$	$a_6$
interior		1/3	14/9	1/9				
node 0	5		197/60	-5/12	5	-5/3	5/12	-1/20
node 1	3/4	1/8	-43/96	-5/6	9/8	1/6	-1/96	

Coefficients for second derivatives  $f''$ .

	$\beta_1$	$\beta_2$	$b_1$	$b_2$	$b_3$	$b_4$	$b_5$	$b_6$
interior	12/97	-1/194	120/7					
boundary	11/12	-131/4	177/16	-507/8	783/8	-201/4	81/16	-3/8

and analogous for second derivatives as well as grid points near the boundary. The constants  $\alpha_j$  and  $a_j$  have to be determined for the boundaries separately. Tyler calculated the respective constants for different orders (up to  $\mathcal{O}(h^{10})$ ) and boundaries in [50].

If we have  $N$  grid points  $x_i = h i$ ,  $0 \leq i \leq N - 1$ , we have  $N$  linear differential equations which can be subsumed to matrices by

$$A_{\text{left}} \mathbf{f}^{(n)} = A_{\text{right}} \mathbf{f} \quad \Rightarrow \quad \mathbf{f}^{(n)} = \left( A_{\text{left}}^{-1} A_{\text{right}} \right) \mathbf{f}$$

with the inverted left-hand matrix  $A_{\text{left}}^{-1}$  which is possible since the determinant is non-zero. If the matrices remain unchanged during the simulation the matrix  $Q := A_{\text{left}}^{-1} A_{\text{right}}$  may be computed before the integration of differential equations and used in each time step to compute the derivatives. To compute the derivative of a two-dimensional field, e.g.  $\psi(X, Z)$ , I can use this matrix to compute it by one simple matrix multiplication. [50] To implement a Dirichlet boundary condition  $\mathbf{f}_{\text{bc}}$  I utilize the approach presented by Carpenter [51] by computing  $Q_{\text{bc}} := A_{\text{left}}^{-1} \mathbf{f}_{\text{bc}}$  for the respective boundary values and add this constant vector to adjust the derivative  $f^{(n)}$  for the boundaries.

In table 2 I present the coefficients for sixth order compact finite difference schemes which I used in the numerical simulations for computing the first and second derivatives. The values are obtained by Tyler in [50].

### 6.3. Pseudo-spectral method

In the following I will present a pseudo-spectral Fourier-Galerkin method to solve the Poisson equation (6.7) in two dimensions with periodicity in one direction. The approach is described in [19–21, 52]. The advantage is that such pseudo-spectral methods are com-

putationally efficient since one only has to compute Matrix multiplications as well as the Fast Fourier Transform algorithm.

In X-direction I employ a Fourier expansion assuming  $M \times N$  grid points  $x_m = m \Delta x$  and  $y_n = n \Delta z$  with grid spacing  $\Delta x$  and  $\Delta z$  and  $0 \leq m \leq M-1, 0 \leq n \leq N-1$ .

$$\tilde{\psi}(x_m, y_n) = \frac{1}{M} \sum_{k=-M/2}^{M/2-1} \widehat{\psi}_k(y_n) e^{-2\pi i \frac{x_m k}{L}} \quad (6.12)$$

with Fourier coefficients  $\widehat{\psi}_{k,n}$  and an analogous expansion for  $\tilde{\omega}_{m,n}$ . I use the respective backward Fourier transformations to transform the fields from Fourier to real space.

I utilize a compact finite difference scheme for the second order derivative in Z-direction with the left- and right-hand matrices  $A_{\text{left}}^0$  and  $A_{\text{right}}^0$  respectively, satisfying

$$A_{\text{left}}^0 F''(X, Z) = A_{\text{right}}^0 F(X, Z) \quad (6.13)$$

for a scalar field  $F(X, Z)$ .

After Fourier transform the Poisson equation (6.7) may be written as

$$\partial_{XX} \tilde{\psi}(X, Z) + \partial_{ZZ} \tilde{\psi}(X, Z) = -\tilde{\omega}(X, Z).$$

Following [20] I now compute the X-derivative analytically using the Fourier expansion (6.12) and the Z-derivative by the compact finite difference scheme (6.13):

$$\sum_{k=-M/2}^{M/2-1} \left[ (\partial_{XX} + \partial_{ZZ}) \widehat{\psi}_k(y_n) e^{-2\pi i \frac{x_m k}{L}} \right] = - \sum_{k=-M/2}^{M/2-1} \left[ \widehat{\omega}_k(y_n) e^{-2\pi i \frac{x_m k}{L}} \right].$$

Since the equation holds for every  $k$  for the Fourier expansion I get

$$\begin{aligned} \partial_{XX} \widehat{\psi}_k(y_n) + \partial_{ZZ} \widehat{\psi}_k(y_n) &= -\widehat{\omega}_k(y_n), \\ \Rightarrow \left( \frac{-2\pi i k}{L} \right)^2 \widehat{\psi}_k(y_n) + \partial_{ZZ} \widehat{\psi}_k(y_n) &= -\widehat{\omega}_k(y_n), \\ \Rightarrow -A_{\text{left}}^0 \left( \frac{2\pi k}{L} \right)^2 \widehat{\psi}_k(y_n) + A_{\text{right}}^0 \widehat{\psi}_k(y_n) &= -A_{\text{left}}^0 \widehat{\omega}_k(y_n) \\ \Rightarrow \widehat{\psi}_k(y_n) &= - \left( -A_{\text{left}}^0 \left( \frac{2\pi k}{L} \right)^2 + A_{\text{right}}^0 \right)^{-1} A_{\text{left}}^0 \widehat{\omega}_k(y_n). \end{aligned}$$

Hence, we have a  $k$ -dependent two-dimensional matrix to compute the Poisson equation in each time-step which can be implemented adjusting the parameters in the described compact finite difference scheme. By applying a backward Fourier transformation on  $\widehat{\psi}_k(y_n)$  we get the stream function  $\psi(x_m, y_n)$ .

## 6.4. Time-stepping

In this section I describe the realization of each integration step. For the time-stepping of the salinity equation (6.9) I follow Ruith and Riaz [19, 20] by utilizing an explicit multi-step, third-order Runge-Kutta scheme introduced by Wray [23] with time step  $\Delta\tau$ .

Following [19, 20] I write equation (6.9) as

$$\frac{\partial S_{i,j}}{\partial \tau} =: F(\mathbf{U}_{i,j}, S_{i,j})$$

and introduce the three steps for  $k \in \{1, 2, 3\}$

$$S_{i,j}^{(k)} = S_{i,j}^{(k-1)} + \Delta\tau \left[ \alpha_k F(\mathbf{U}_{i,j}, S_{i,j}^{(k-1)}) + \beta_k F(\mathbf{U}_{i,j}, S_{i,j}^{(k-2)}) \right],$$

with  $S_{i,j}^{(0)}$  the salinity from the former time-step and  $S_{i,j}^{(3)}$  the final salinity using the coefficients:

$\alpha_1 = 8/15$	$\alpha_2 = 5/12$	$\alpha_3 = 3/4$
$\beta_1 = 0$	$\beta_2 = -17/60$	$\beta_3 = -5/12$

In every time-step I compute the vorticity  $\omega$  using (6.6), then solve the Poisson equation (6.7) using the described pseudo-spectral method by transforming the vorticity  $\omega$  into Fourier space and computing the stream function and transform it back. I make use of the Fast Fourier Transform algorithm. By applying the compact finite difference schemes to compute the derivatives as well as the analytical derivatives of  $\psi^0(X, Z)$  I then compute the velocity in real space using equation (6.8). Finally I use the described Runge-Kutta method to compute the evolution of the salinity distribution  $S(X, Y, \tau)$ . (Compare [19–21, 53])

The grid size is chosen so that  $\Delta X$  and  $\Delta Y$  are in order  $\mathcal{O}(0.02)$  to reduce computation time while being small enough to represent the occurring characteristic length scales. The time steps  $\Delta\tau$  are computed using the Courant–Friedrichs–Lewy condition [48]

$$C = \frac{U_{\max} \Delta\tau}{\Delta X} \leq C_0.$$

The condition  $C_0$  for stability is of order  $\mathcal{O}(1)$  and chosen to be 0.1 which leads to stable systems. Here, I use the highest occurring velocity in the system  $U_{\max}$  which is computed every 10 time steps. The validation of the code is done by computing the growth rates for small periodic perturbations and comparing the numerical simulations with the theoretical analysis in section 3. This is described in the subsequent section.

## 6.5. Validation of growth rates

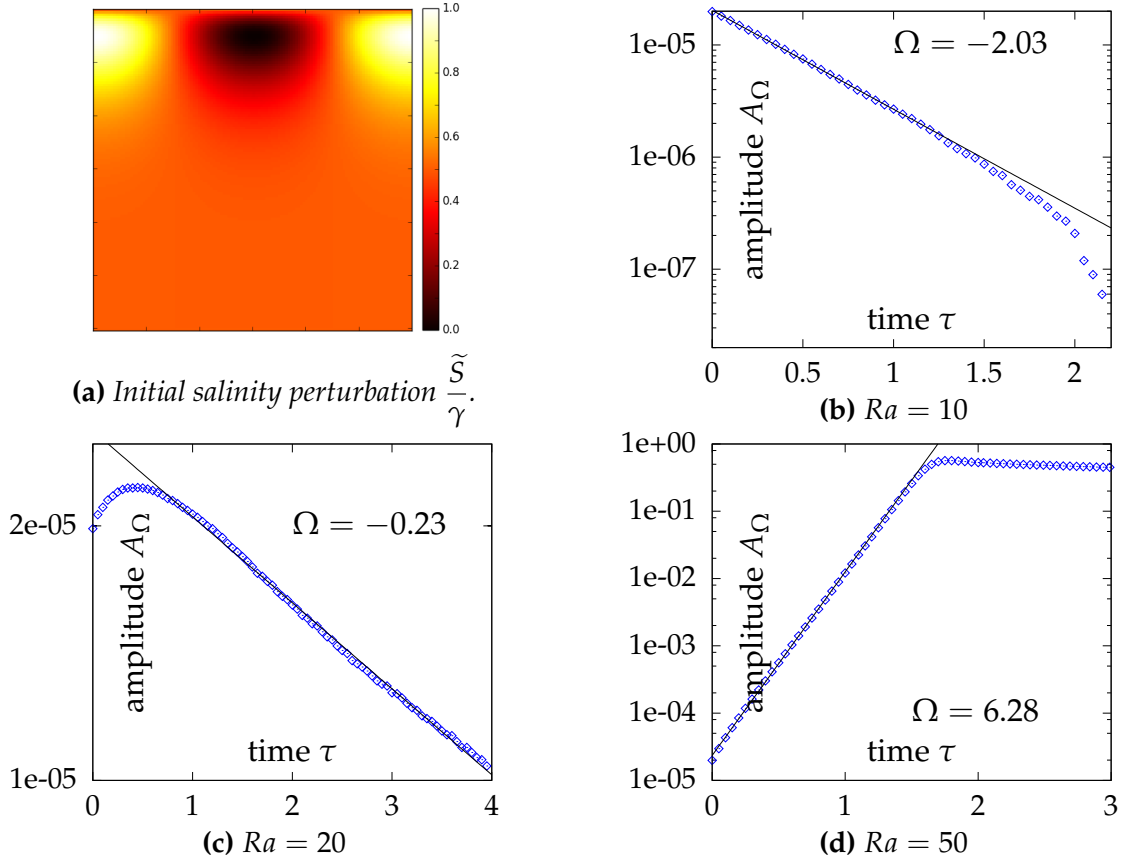


**Figure 20:** Figure 20a displays the basic initial salinity perturbation which is added to the steady-state. In figure 20b to 20d I show the amplitude  $A$  of that mode as a function of time for the height  $H = 12$ , the wavenumber  $a = 1.7637$  and different Rayleigh numbers, as well as a linear fit of the exponential regime to get the growth rate in the exponential regime.

In the following I will present a validation of the implementation of the model for periodic perturbations of small amplitude using the semi-analytical linear stability analysis shown in section 3. This approach to validate the implementation, by comparing the growth rates for small perturbations with theory is widely used as for instance in [19, 20, 47, 53]. As we are interested in the instability of the system under perturbations, which is expected to drive the pattern formation on the surface, validation of the growth rates

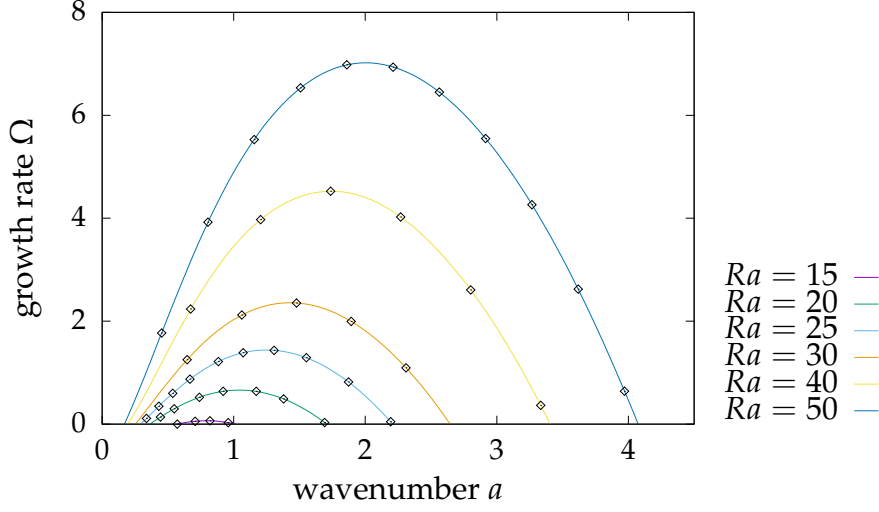


**Figure 21:** Comparison of theoretical and numerical growth rates  $\Omega$  as a function of the wavenumber  $a - a_c$  (adjusted for critical wavenumber) for the height  $H = 12$  and different Rayleigh numbers  $Ra$  for a top boundary condition of uniform vertical velocity  $U_z$ . The black squares represent the numerical results and the curves the theoretical values computed in chapter 3.

in the simulation seems like a good choice. I will compare the theoretical and numerical dependency of the growth rates of the wavenumber  $a$  for small perturbations of salinity added to the exponential steady-state solution of the finite system with width  $L$  and height  $H$ . Assuming  $S = 1$  at the top boundary ( $Z = 0$ ) as well as a uniform evaporation rate  $E = E_0$  and  $S = 0$  at the bottom boundary ( $Z = -H$ ) I utilize the steady-state solution of equation (6.10) and the salinity perturbation

$$\tilde{S}(X, Z) = -\gamma Z \left( \frac{e^Z - e^H}{1 - e^H} \right) \cos(2\pi a X)$$

shown in figure 20a.  $\gamma$  is the amplitude of the perturbation and chosen to be  $1 \cdot 10^{-5}$  that it is small enough to be linear and large enough to avoid floating errors. It is a periodic cosine function in horizontal  $X$ -direction. The vertical dependence of the perturbation is chosen arbitrary but consistent with the Dirichlet boundary conditions and similar to the most unstable modes in the linear stability analysis exemplary shown in figure 8.

The height of the two-dimensional system is constant,  $H = 12$ , which is large enough that the resulting growth rates are no function of height. I checked this by computing the growth rates for  $H = 16$  as well and got the same result with relative deviations of order  $10^{-5}$ . The horizontal length  $L$  is  $L = 2\pi/a$ , which corresponds one wavelength. Since the system is periodic in the  $X$ -direction and I have no random perturbations I do not need to choose a larger system.

In figure 20b to 20d I display the amplitude  $A_\Omega(\tau)$  of the perturbations as a function of the time for systems of different Rayleigh number  $Ra$ . To compute the amplitude I determine the maxima and minima of the sinusoidal perturbation. Using  $A_\Omega(\tau) \propto e^{\Omega\tau}$  I can measure the growth rate of the perturbations. Hereby I have to consider the following difficulties: When the amplitude is too small the discretization may influence the slope, as shown in figure 20b; in some cases the amplitude does have a transient, as for instance in figure 20c where the amplitude is increasing first and then decreasing exponentially. This may be an effect of the transient behavior of the vertical perturbation dependence; Finally, if the amplitude is increasing and reaches order an of 1, non-linear effects are becoming important as shown in figure 20d.

The resulting growth rates and the comparison with the analytical results from chapter 3 are shown in figure 21. There is a nearly perfect coincidence with a relative error in the order of magnitude of  $10^{-2} - 10^{-3}$ . Hence, the implementation is validated for small amplitudes and further investigations are expected to give reasonable results.





## 7. Results from numerical simulation

In the following chapter I investigate the dynamics of saline-gradient driven convection in a two-dimensional, finite system utilizing the numerical simulation of the previous chapter. The aim of the simulations is to simulate the quasi two-dimensional experimental systems in Hele Shaw cells because numerical simulation allows one to investigate the parameter space more systematically and analyze connection between surface structures and subsurface flow dynamics.

For that purpose I firstly analyze the development of the system in the steady-state given in equation (6.10). If the density difference of the top and bottom boundary  $\Delta\rho$  is large enough and thereby the Rayleigh number  $Ra$  is larger than the critical Rayleigh number  $Ra_c$  the system is not stable and I expect downwelling fingers of higher salt concentration respectively salinity [13]. I use the numerical simulation to investigate the wavelength and the front velocities as a function of the Rayleigh number of the system for early times. I expect the wavelength of the fingers to be in the same order of magnitude as the most unstable mode calculated in the linear stability analysis 3 since the wavelength with largest growth rate for small perturbations will dominate the early time behavior. The fingers will coarsen and thereby increase the wavelength until convection cells as a dynamic equilibrium will develop. I show the exemplary qualitative development from the steady state to convection cells.

Since the time scale from the setup of the Hele-Shaw cell until the salt concentration near the surface reaches saturation – which is the precondition for the considered coloring experiments – is much larger than the time scale of the advection in the experiments itself we assume that convection cells are already developed. Additionally the qualitative behavior of the visualized flow in the Hele-Shaw cells shows characteristics of convection cells since it exhibits similar up- as well as down-welling regimes.

Hence, we primarily care for the flow properties of the convection cells in the system and need to establish measures to compare the numerical simulation with the experimental data. Since the velocity and the wavelength of the convection cells in the experiments is taken at half height we investigate those measures in the simulation as well. I compute the regime of wavelengths  $[\lambda_{min}, \lambda_{max}]$  for which the convection cells in the two-dimensional system are stable. Due to wrong approximations which we have done initially I investigated the wrong regime of the finite system height  $H$ . Hence, further study are necessary for a robust validation of the numerical simulation with experimental data, but preliminary results can be shown.

To investigate the real-world salt playa we need to study whether the subsurface con-

vection cells and their wavelength is robust for changing external conditions such as temperature and humidity changes. Hence, the analysis of the stable regime of already developed convection cells is important for the understanding of their behavior.

Finally I present some preliminary results regarding the connection of the salt ridges to the surface and the subsurface dynamics. For that purpose I analyze whether variation in the evaporation rate at the top boundary does have an influence on the convective behavior and pins the convection cells and the surface patterns. Such pinning is crucial for our hypothesis that convection cells play a major role in the development of the salt ridge patterns. In the surroundings of the salt ridges the salt crust is patchy and cracked while we observe a thick and continuous salt crust in the shallow interstice of the patterns. The evaporation rate is larger for the patchy regions because the salt crust acts as a wick to increase evaporative surface while the crusty region blocks the evaporation as shown by Eloukabi [9]. If the upwelling regime of the convection cells occurs below the salt ridges pinning would compensate for spatial deferrals of the convection cells due to external conditions. Without pinning and with spatial shifts of the convection cells the formation of the salt ridges might not occur.

### 7.1. Fingering behaviour

The aim of this section is to analyze the fingering behavior for early times. Fingering is a well-known phenomenon occurring for instabilities between two miscible fluids [17] or buoyancy driven instabilities for our system [13] as well as the coarsening of the occurring fingers.

In figure 22 I display an exemplary development of the finite system in the numerical simulation from the steady-state to the emergence of convection cells.

We observe an initial instability for the time  $\tau = 0.1$  and the emergence of fingers for  $\tau = 0.2$ , their coarsening for  $\tau = 0.4$  as well as the development of convection cells for later times.

Since I aim to analyze the qualitative early time behavior of the fingering I am interested in the wavelengths and the velocities of the occurring fingers as a function of the instability parameter – the Rayleigh number  $Ra$ .

For that purpose I analyze a system of height  $H = 8$  and large horizontal length  $L \approx 40$  in  $X$ -direction and use the steady-state given in equation (6.10) as initial condition. I impose random white noise according to equation (6.11) with an amplitude  $\gamma = 0.01$  onto the steady-state and analyze the development for different Rayleigh numbers by introducing the following measure: I let the system evolve until one of the fingers reaches the height  $Z = -2$  – the salinity maximum at  $Z = -2$  exceeds the threshold of 0.5.

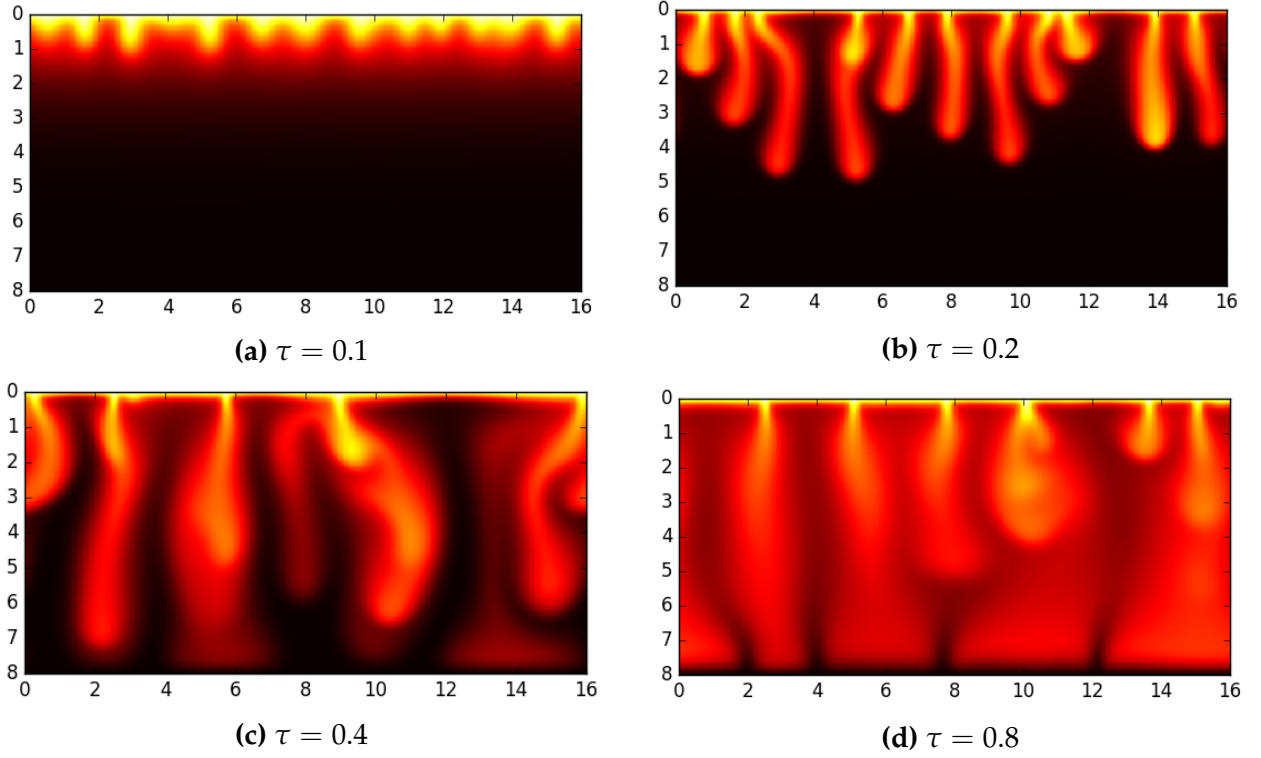
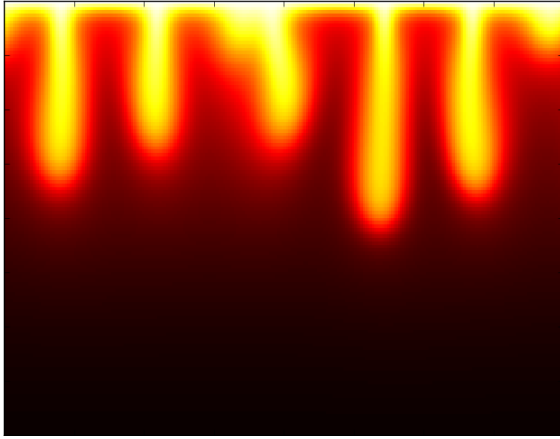


**Figure 22:** Qualitative development of the salinity from steady-state for early times with a Rayleigh number  $Ra = 200$ . For this simulation I impose random white noise according to equation (6.11) with amplitude  $\gamma = 0.01$ .

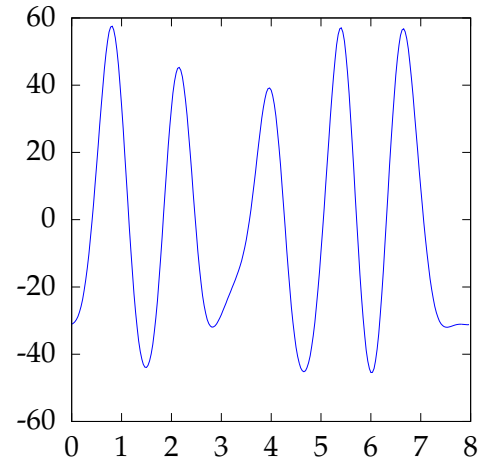
Then I take the horizontal profile of the vertical velocities at the height  $Z = -1$  and determine the number of maxima to compute the wavelength and take the velocities in its maxima and minima to get the mean front velocities. In figure 23a I display an exemplary concentration profile at the time when the threshold is exceeded. In figure 23b is the respective profile of the vertical velocities.

In figure 24 I display the neutral stability curve, the most unstable mode from the linear stability analysis in chapter 3 and the wavenumber of the fingers as a function of the Rayleigh number  $Ra$ . This allows us to compare the spacing of the fingers with the wavenumber of the fastest growing perturbation. The latter is only valid for small scale perturbations. In accordance with my expectation the wavenumber of the fingers in early times are matching the linear stability analysis. For  $Ra < Ra_c$  the steady-state is stable and hence no fingers occur.

In figure 25 I present the the velocity dependence at the height  $Y = -1$  of the Rayleigh number  $Ra$ . For that purpose I compute the mean average front velocities in up- as well as down-welling directions. The downwelling front velocities are significantly larger than the upwelling velocities since we analyze the early-time behavior of the down-welling



(a) Salinity profile for  $Ra = 200$ .



(b) Vertical velocity  $U_Z(X)$  at  $Z = -1$ .

**Figure 23:** Fingering for a system with Rayleigh number  $Ra = 200$  at the time  $\tau = 0.128$ . 23b shows the vertical velocity profile at a specific height  $Z = -1$ . This state fulfills the condition that at least one of the fingers reached the height  $Z = -2$ .

fingering. When plotting the vertical front velocities  $U_Z$  divided by the relative Rayleigh number  $Ra - Ra_c$  in figure 26 the numerical values fluctuate around a constant value. If I divide the velocities by the Rayleigh number  $Ra$  the adjusted velocities will significantly drop for small Rayleigh numbers.

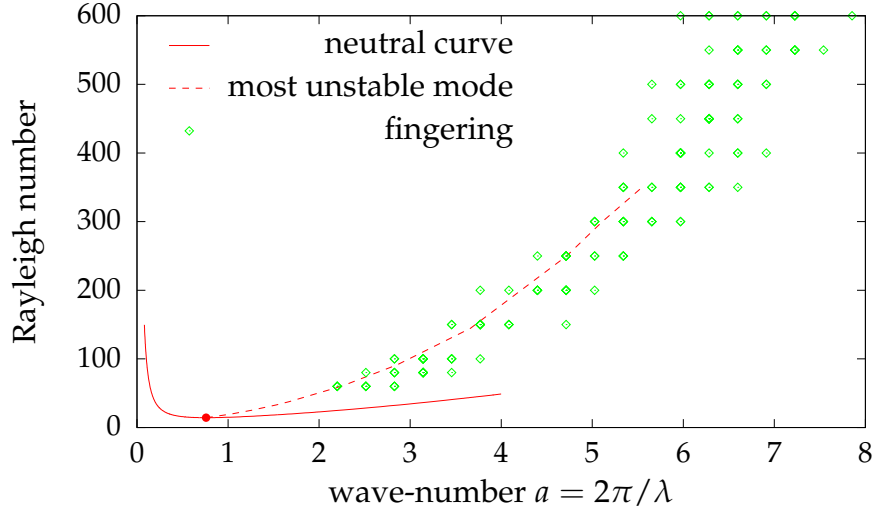


**Figure 24:** neutral stability curve and most unstable mode from the theoretical linear stability analysis in chapter 3 and the wavenumber  $a$  of the occurring fingers as a function of the Rayleigh number  $Ra$ . The wavenumber is determined at height  $Z = -1$  when the salinity exceeds the threshold of 0.5 at  $Z = -2$  as shown in figure 23.

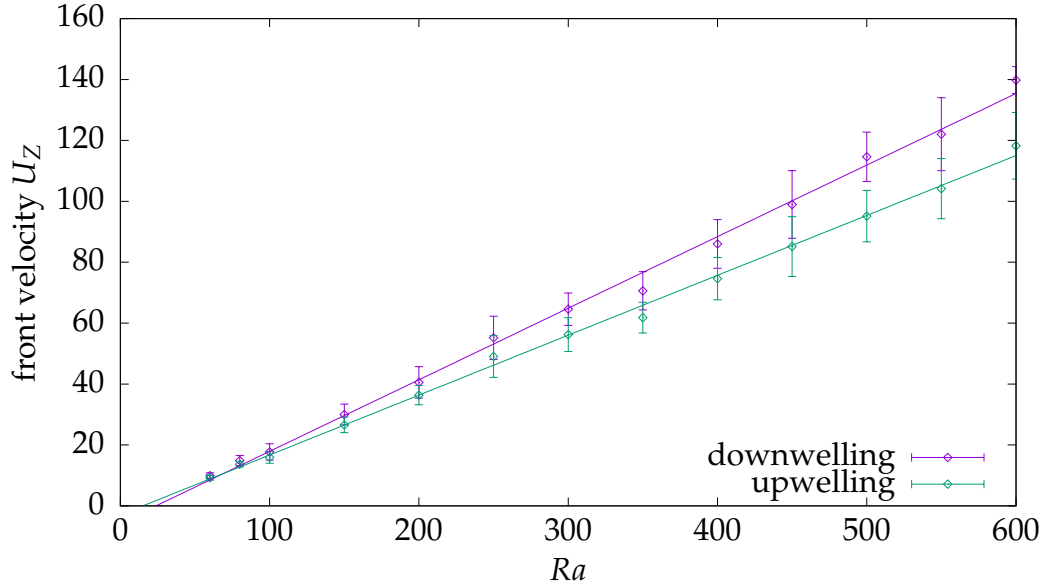


**Figure 25:** Vertical front velocities  $U_Z$  of the early-time fingering for the up- and down-welling direction as a function of Rayleigh number  $Ra$ . The velocities are determined at height  $Z = -1$  when the salinity exceeds the threshold of 0.5 at  $Z = -2$  (compare figure 23).

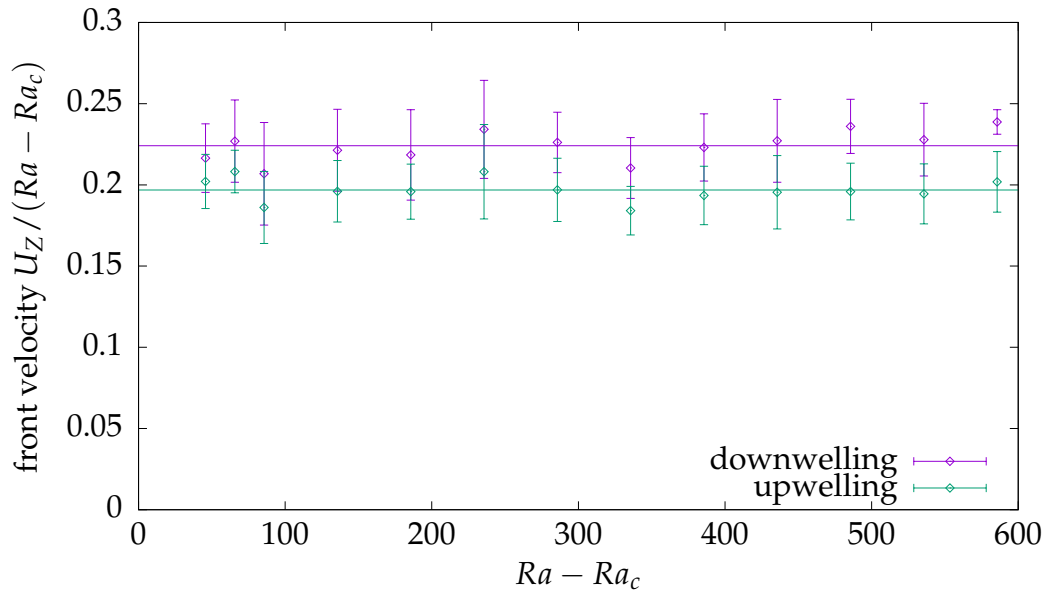


**Figure 26:** Vertical front velocities  $\frac{U_Z}{Ra - Ra_c}$  of the early-time fingering for the up- and down-welling direction as a function of Rayleigh number  $Ra$ . Compare figure 25 .

## 7.2. Investigation of convection cells

In this section I present first results of the numerical simulation of convection cells in the two-dimensional system. Since we have experimental measures regarding the wavelength of the occurring convection cells as well as the maximal front velocities at half height I consider these measures for my numerical study, too. In this preliminary study I do not focus on the influence of the height of the system which is an important question for subsequent work with the numerical simulations.

For our hypothesis for the real-world system the connection between the salt ridges on the surface and the subsurface convection cells is crucial. Hence, the number of convection cells in the system needs to be robust against small changes of external conditions such as the evaporation rate. I investigate the wavelength regime for which a specific number of convection cells in a finite system of length with periodic boundary conditions in horizontal directions is stationary. Within this regime changes of external conditions will not necessarily change the number of convection cells.

For that purpose I simulate a system of height  $H$  and length  $L$  with  $N$  stationary convection cells as in figure 27 as initial condition and let the system evolve in time to check after a time of  $\tau = 20$  whether the convection cells stay stationary and the number of convection cells does not change.

By simulating the stationary convection cells for different lengths  $L$  of the system, different Rayleigh numbers  $Ra$  and number of convection cells I can compute the wavelength regime  $[\lambda_{min}, \lambda_{max}]$  for stationary convection cells. These regimes are shown in figure 28. For a given length  $L$  different number of convection cells  $N$  can be stationary so that changes of external conditions are not necessarily changing the convective behavior qualitatively and the system shows hysteresis behavior.

For larger Rayleigh number  $Ra$  the wavelength of convection cells is decreasing as well as the width of the stationary regime  $[\lambda_{min}, \lambda_{max}]$ . The lower limit depends on the number  $N$  of stationary convection cells. For  $N = 1$  the number of cells cannot reduce but the system slows down more and more when reducing the length. For a larger number of cells there may be a transition to  $N - 1$  stationary cells. The respective change in wavelength is smaller for larger  $N$ . Further investigations of the stationary regime for large  $N$  and large heights  $H$  are important.

In figure 29 I present the vertical front velocity of the convection cells at half height as a function of the wavelength for different Rayleigh numbers  $Ra$ . The front velocities are increasing from 0 for smaller wavelengths and after reaching a maximum slowly decaying for larger wavelengths until the convection cells are not stationary anymore. The small velocity regime only occurs for  $N = 1$  since  $\lambda_{min}$  is larger for  $N > 1$ . We observe a slow-

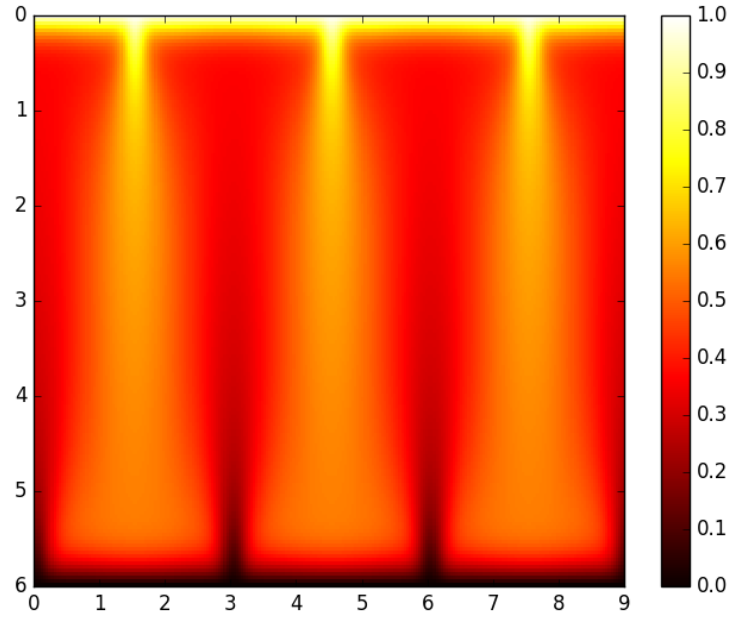


**Figure 27:** Exemplary convection cells for a Rayleigh number of  $Ra = 200$ . The convection cells are used as initial condition for systems of different lengths  $L$  and Rayleigh numbers  $Ra$  to investigate the wavelength regime  $[\lambda_{min}, \lambda_{max}]$  for which the convection cells stays stationary as well as the front velocities of the convection cells.

down of the stationary convection cell when reducing the wavelength until it approaches the exponential steady-state of the system.

Since the front velocity for larger wavelengths in this regime is nearly constant I choose the maximal value of those velocities as a function of Rayleigh number  $Ra$  to compare these values with the experimental results. The results are shown in figure 30.



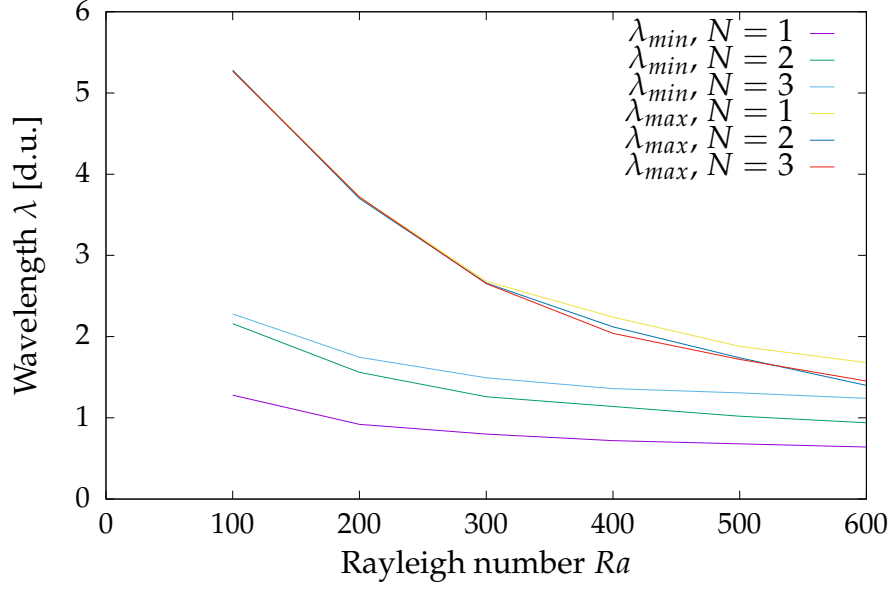


**Figure 28:** Shown are the minimal and maximal wavelengths  $\lambda_{\min}$  and  $\lambda_{\max}$  for which a convection cell as initial conditions stays stationary as a function of the Rayleigh number  $Ra$ . For that purpose I used  $N$  convection cells in figure 27 as initial condition for a height of  $H = 8$  and different lengths  $L$  of the cell, let it develop for  $\tau = 10$  and investigate the stability of the convection cells by checking whether the number of maxima at all heights stays  $N$ . I scanned the parameter space and computed the minimal and maximal wavelength regime of stability.

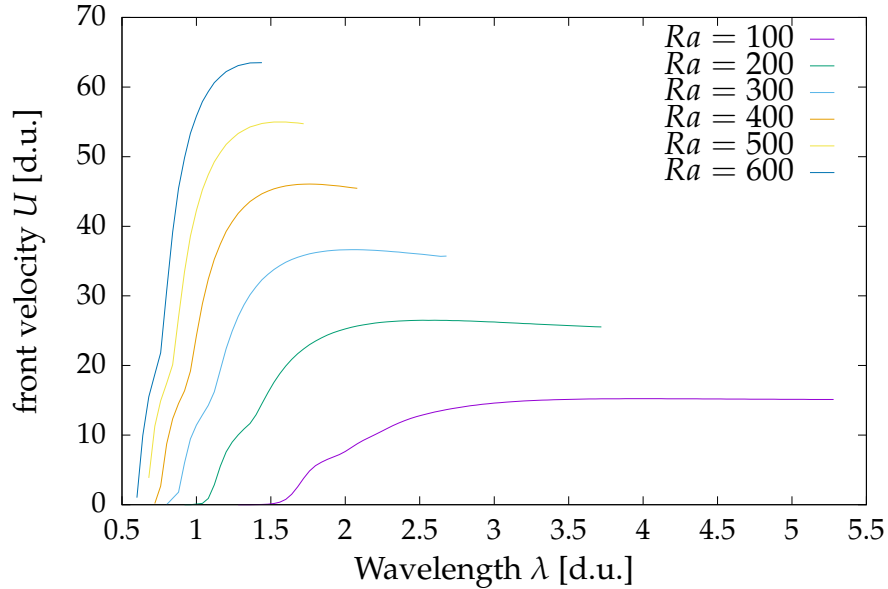


**Figure 29:** Shown is the vertical front velocity  $U_z$  at half height of stable convection cells as a function of the wavelength  $\lambda$  for different Rayleigh numbers  $Ra$  within the stable regime  $[\lambda_{\min}, \lambda_{\max}]$ . For that purpose I used an initial condition with one convection cell because those stay stable for smaller wavelengths. The velocity dependence for other  $N$  is equivalent.

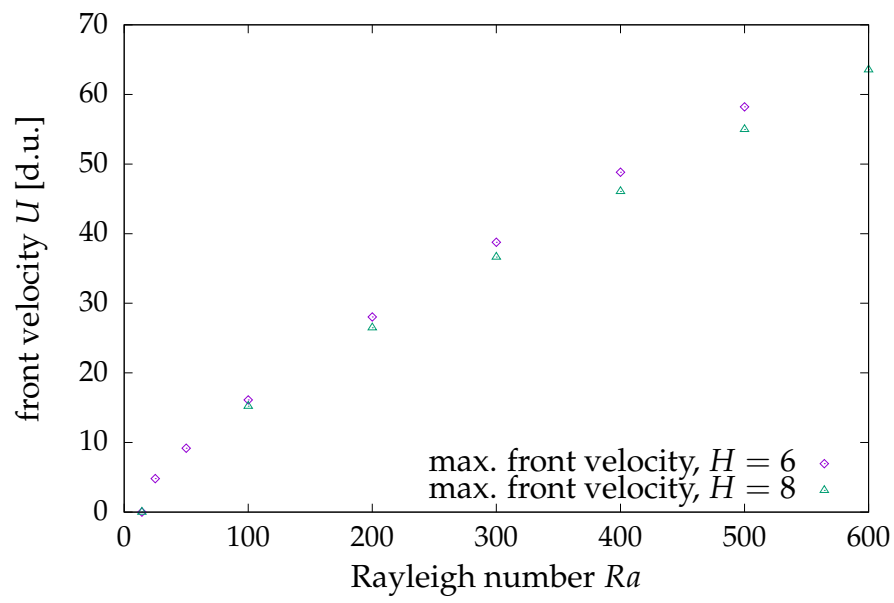


**Figure 30:** Shown is the maximum of the curves in figure 29 as a function of the Rayleigh number  $Ra$ .

### 7.3. Comparison with experimental data

In this section I present the comparison of the experimental data from chapter 4 with the results from the numerical simulation because this is crucial for validating the simulation. The simulation aims to simulate the two-dimensional experiment and I use the wavelength of convection cells as well as their front velocities at half height for comparison.

Firstly, I have to convert the experimental data to non-dimensional units. For that purpose I need estimations for the physical constants.

The molecular diffusion constant  $D$  for sodium chloride in water at 25 °C is approximately  $D = 0.805 \times 10^{-9} \text{ m}^2/\text{s}$  [43]. As stated above in section 4.2 the dispersion can safely be neglected. Since our length scale is  $L = \frac{D}{E_0}$  and the evaporation rate  $E_0$  is 0.2 to 4  $\mu\text{m}/\text{s}$  we have unit lengths of order 0.2 to 4 mm. With heights of the sand of about 15 cm this results in dimensionless heights  $H \approx 40$  to 750 which is much larger than the height regimes I considered in the first numerical study of convection cells in the former section. Nevertheless I will compare the experimental data which should be interpreted cautiously. The time scale  $T = \frac{D}{E_0^2}$  then ranges from 50 to  $20 \times 10^3 \text{ s}$ .

To compute the Rayleigh number using equation (2.13)

$$Ra = \frac{\Delta\rho g \kappa}{\varphi E_0 \mu_0}$$

I estimate  $\Delta\rho$  for systems with saturated salt water at the top and background salt concentration  $c_b = \frac{25 \text{ g salt}}{1 \text{ kg water}}$  at the bottom boundary condition by using the relation (2.8) and get  $\Delta\rho \approx 178 \text{ kg}/\text{m}^3$ . The permeability is  $\kappa \approx (1.67 \pm 0.12) \times 10^{-11} \text{ m}^2$  [39] and the viscosity  $\mu_0$  for 25 °C for fresh water is  $\mu_0 \approx 1 \times 10^{-3} \text{ kg}/(\text{m s})$ . [35]. Using these values the Rayleigh numbers range from 20 to 600 while the evaporation rate is the only changing parameter for our experimental data since the other constants are not modified.

The advective velocity of the convection is non-dimensionalized by using the evaporation rate  $E_0$ .

Firstly I compare the experimental data with the theoretical neutral stability curve from the linear stability analysis in chapter 3. The results are plotted in figure 29. In contradiction to the expectation many experimental data points are outside of the neutral stability curve in the stable regime. Hence, there is need to investigate this divergence from theory. In figure 32 I compare the experimental data for the wavelengths of the convection cells with the stable wavelength regime from the numerical simulation. The experimental data are not within this stable regime and there even is a deviation of one order of magnitude.

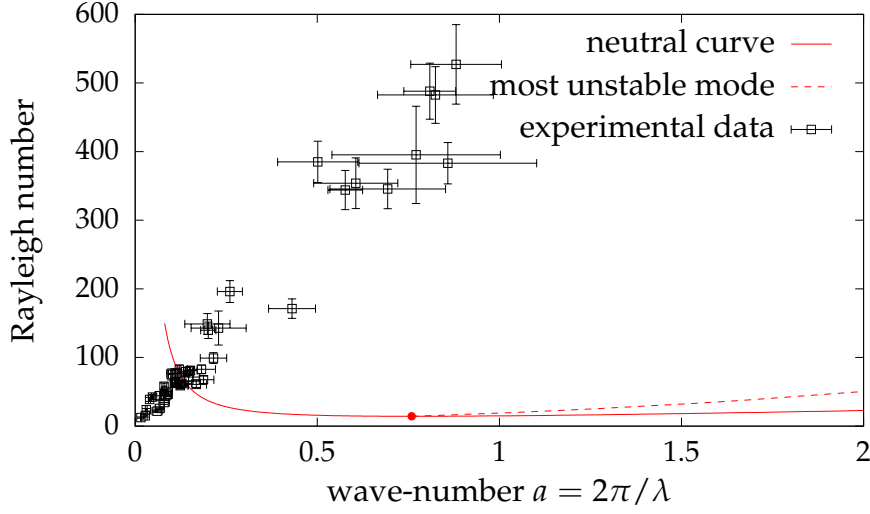


**Figure 31:** Shown is the neutral stability curve from theoretical linear stability analysis as well as the wavenumber  $a$  of the occurring convection cells in the experiment in dimensionless units for different Rayleigh numbers  $Ra$ .

Since I investigated a height regime of  $H = \mathcal{O}(10)$  in the simulation while  $H = \mathcal{O}(500)$  in the experiments further investigation may help to match the experimental data and the simulation.

In figure 33 I show that the vertical front velocities of the convection cells is in the same order of magnitude and having the same trend for increasing Rayleigh numbers although some of the experimental data points are outliers.

All things considered more investigation of the simulations for larger dimensionless heights is needed to validate the simulation with the experimental data.

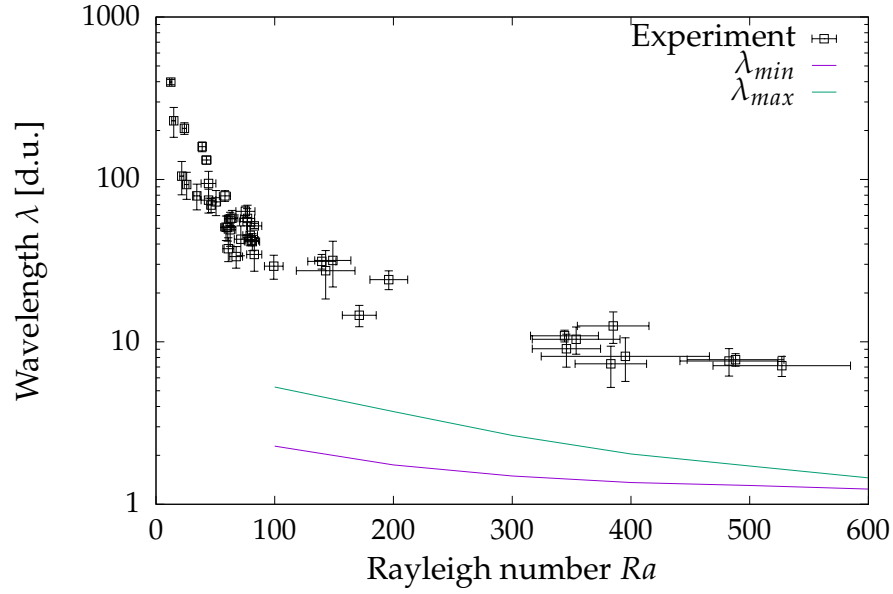


**Figure 32:** Shown is the experimental wavelength of the occurring convection cells in dimensionless units as well as the stationary wavelength regime  $[\lambda_{min}, \lambda_{max}]$  from the simulation for  $H = 8$  (too small).

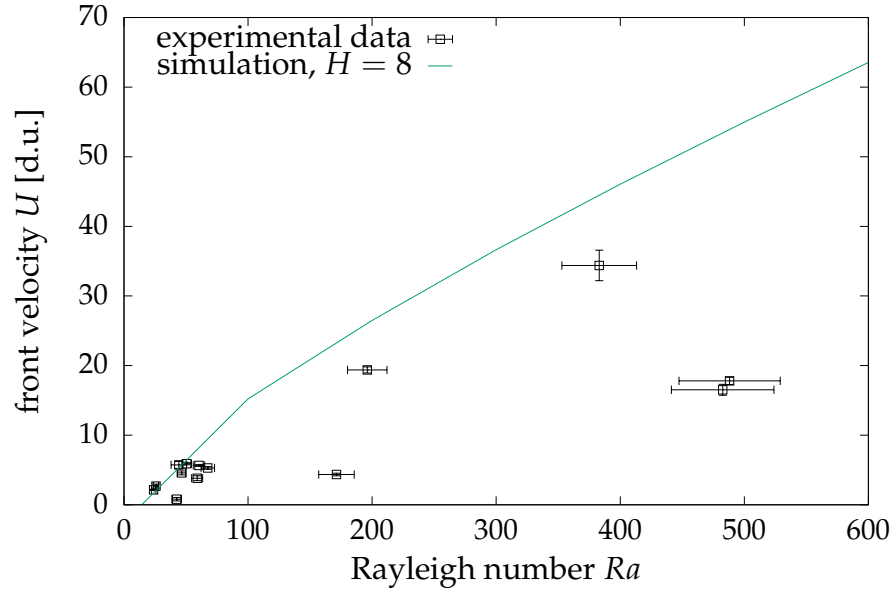


**Figure 33:** Shown is the vertical front velocity of the convection cells in the experiment as well as the numerical results for a height of  $H = 8$  as shown in figure 30.

## 7.4. Investigation of pinning behaviour

In this section I will use the numerical model to study the connection of the salt ridges and the subsurface convection. Our hypothesis claims that the salt ridges causes an increase of evaporation rate because the surface is more patchy there while the evaporation in the regions between the salt ridges is partially blocked. We further claim that these variations of evaporation rates are pinning the subsurface convection cells. The upwelling regimes of the convection cells are expected to match the maxima of evaporation.

For that purpose I will use a simplified model of those variations by imposing a sinusoidal variation of the evaporation rate  $E(X)$  at the surface with  $E(X) = 1 + A \cos(a_p X)$  with amplitude  $A$  and wavenumber  $a_p$ . Besides the bottom boundary condition is set to have constant vertical flux  $E(X) = 1$ . In figure 34 I plot the exemplary evaporation at the surface. I present a preliminary study of the pinning effect to investigate whether the effect is relevant.

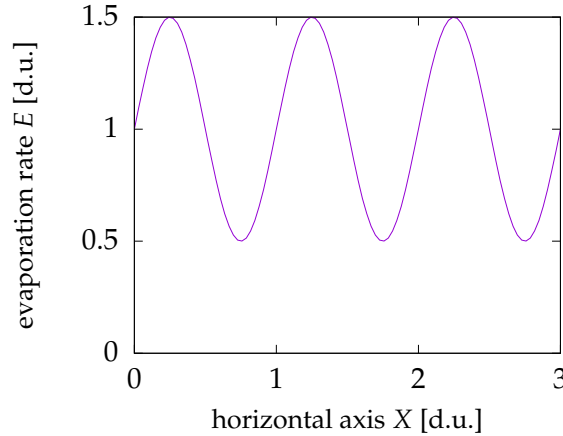


**Figure 34:** Shown is the variation of the evaporation rate  $E(X) = 1 + A \cos(a_p X)$  at the surface for the study of pinning in this section. The shape is sinusoidal with an amplitude of  $A$  and a wavenumber  $a_p$ .

According to the equations (6.6) to (6.9) for the implementation of the system I have to define an analytical function  $\psi^0(X, Z)$  causing the specific boundary conditions. I define

$$\psi^0(X, Z) := \frac{A}{a} \sin(a_p X + \varphi_0) \left[ \frac{1}{2} \cos\left(\frac{\pi Z}{H}\right) + \frac{1}{2} \right]. \quad (7.1)$$

with a phase shift of  $\varphi_0$  and a vertical component decreasing from 1 at  $Z = 0$  to 0 at  $Z = -H$ . This ensures the sinusoidal top and uniform bottom boundary condition for the vertical velocity. Using this definition I need to compute  $\omega_0(X, Z)$  and  $\mathbf{U}_0(X, Z)$  ana-

lytically based on definition (7.1)

$$\omega_0(X, Z) = -\nabla^2 \psi^0(X, Z),$$

$$\mathbf{U}_0(X, Z) = \left( -\frac{A \pi}{2a_p H} \sin(a_p X + \varphi_0) \sin\left(\frac{\pi Z}{H}\right), \frac{A}{2} \sin(a_p X + \varphi_0) [\dots] \right).$$

Using these boundary conditions I can investigate the pinning behavior for a sinusoidal evaporation rate.

Firstly I investigate the behavior for a convection cell developing from steady-state. I use the steady-state with random-noise of amplitude  $\gamma = 0.01$  and let the system evolve for a specific time so that a stationary convection cell develops. I determine the relative phase of the upwelling regime and the upwelling region of the evaporation itself. In figure 35 I display the results.

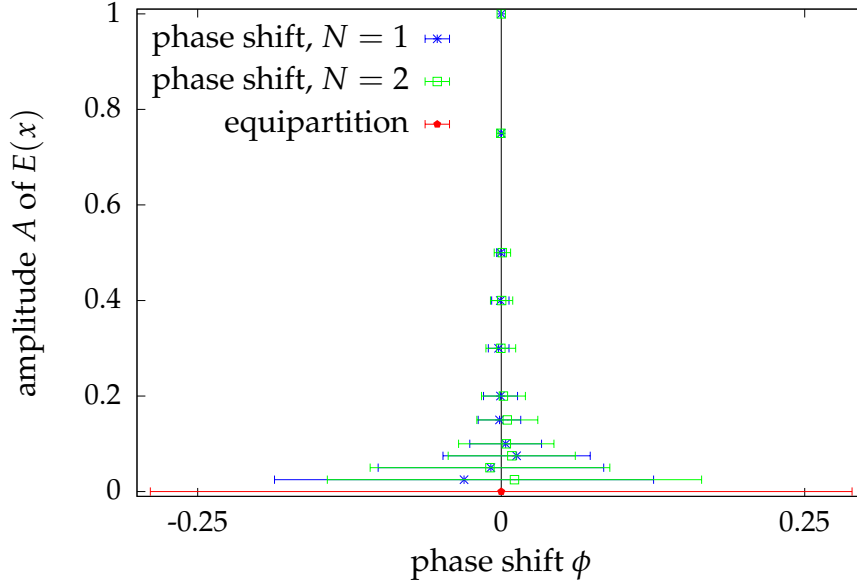


**Figure 35:** Relative phase of upwelling of developing convection cell to the maximum in evaporation rate  $E(X)$  as a function of its amplitude  $A$  with  $E(X) = -1 - \cos(a_p X)$  as well as theoretical expectation for equipartition for  $N$  convection cells and a system size  $H = 6$  and  $L = 2.4 N$  because in that case the convection cells are stationary. The simulation time is  $\tau = 3$  and the Rayleigh number is  $Ra = 200$ . In the diagram I plot the mean as well as the standard deviation after running the simulation 100 times.

We see that for larger amplitudes the standard deviation of the relative phase  $\Delta\phi$  is decreasing while its mean is  $\Delta\phi \approx 0$ . Hence, I can state that we observe pinning. The upwelling regimes of evaporation rate and convection matches while larger amplitudes enhance the pinning effect as expected.

Secondly I investigate stationary convection cell as initial condition with a phase  $\phi_0$  relative to an imposed evaporation rate. This aims to analyze the evolution of the relative

phase of time. In figure 36 I show the time development of the relative phase for some exemplary systems.

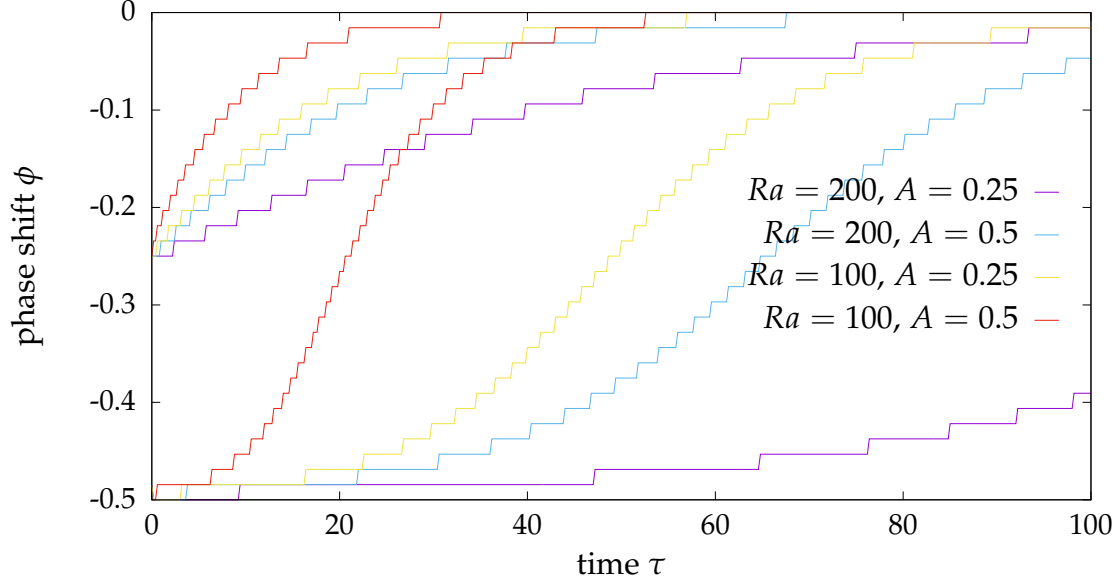


**Figure 36:** Time development of the relative phase  $\phi$  of the upwelling of a convection cell at half height to the maximum in evaporation rate  $E(X)$  for different Rayleigh numbers  $Ra$ , initial phase  $\phi_0$  and amplitudes  $A$  of the evaporation rate  $E(X) = 1 + A \cos(a_p X)$ . I use convection cells and evaporation rate variations with the same wavenumber  $a_p = a$ . A phase of 0.5 corresponds to an upwelling regime directly below the minima of the evaporation rate and 0 corresponds to an upwelling regime matching the maxima.

It can be seen that for all cases the relative phase is approaching 0 but the time the equilibration takes depends on the amplitude of the evaporation rate variations as well as the Rayleigh number. To investigate the pinning efficiency as a function of Rayleigh number  $Ra$  and amplitude  $A$  I use an initial relative phase of 0.5 which corresponds to an upwelling regime of the convection cells below the minima of the evaporation rate. Then I simulate until the relative phase undercuts the threshold 0.02. This time ( $\tau_{0.02}$ ) as a function of Rayleigh number is shown in figure 37.

The time to undercut the threshold  $\tau_{0.02}$  increases for larger Rayleigh number and decreases for larger amplitudes  $A$ . Hence, the pinning efficiency increases for larger amplitudes as expected.

Finally I investigate whether the wavelength regime of stationary convection cells as described in the previous section is changing if one imposes an amplitude  $A > 0$  to the evaporation rate variations  $E(X)$ . The results are shown in figure 38.

The wavelength regime  $[\lambda_{min}, \lambda_{max}]$  is not changing drastically and  $\lambda_{max}$  is slightly decreasing for  $Ra = 200$  if the mean evaporation rate is constant. This suggests that the stability of convection cells is not increasing for sinusoidal evaporation rate variations.



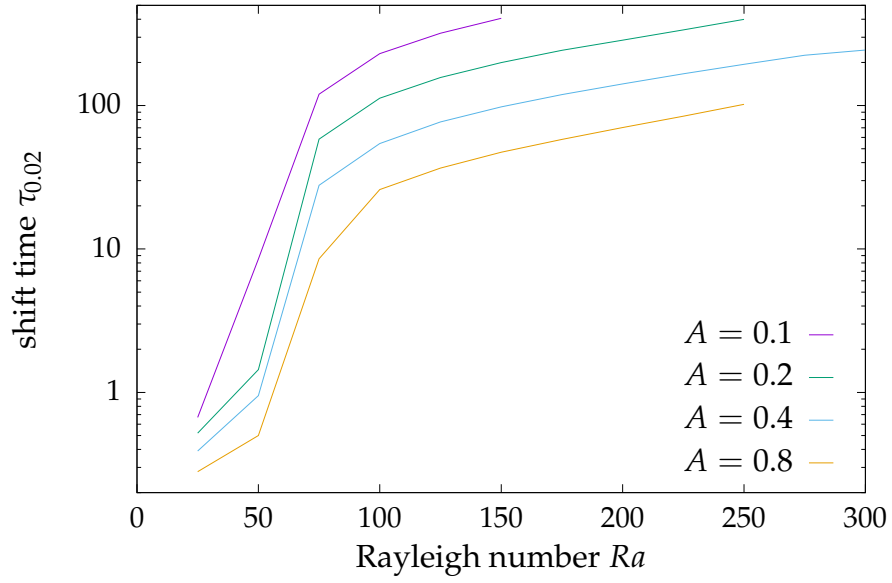


**Figure 37:** Shown is the pinning efficiency as a function of Rayleigh number for different amplitudes  $A$ . I use the measure that the relative phase undercut the threshold 0.02 using an initial phase of 0.5 and a height of  $H = 8$ .

This preliminary study shows that the pinning is a relevant effect and variations in evaporation rate may constitute a relevant factor in connecting the salt ridges and the subsurface convection and pinning the convection cells.

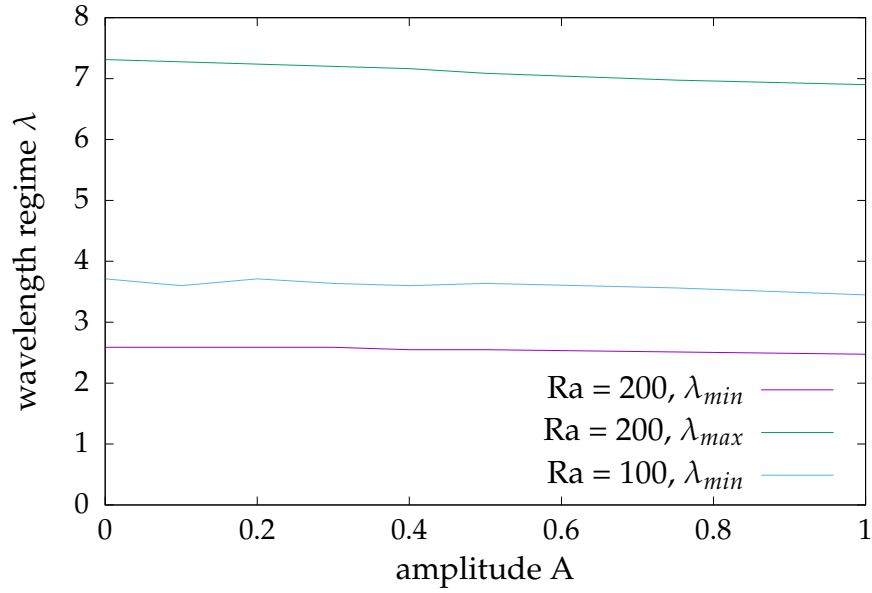


**Figure 38:** Shown is the wavelength regime  $[\lambda_{min}, \lambda_{max}]$  with stationary convection cells for  $Ra = 200$ ,  $N = 3$  cells, a height  $H = 8$  as a function of evaporation rate amplitude  $A$ . The wavenumber  $a$  is the same for the evaporation and the convection cells. For  $Ra = 100$  I only computed  $\lambda_{min}$ .

## 8. Summary

The aim of this thesis is to broaden the understanding of the development of polygonal salt ridge patterns in salt playa. For that purpose I focus on the theoretical investigation of the linear stability as well as implementing a two-dimensional numerical model to simulate respective two-dimensional experiments.

In chapter 2 I firstly sketch the derivation of the differential equation governing the advection-diffusion dynamics of saline water in porous media. Besides the advection-diffusion equation, non-compressibility, the *Darcy Law* is describing the momentum conservation of fluids in porous media. I present a salinity formulation of the differential equations and introduce a Non-dimensionalization of differential equations. Using the Boussinesq approximation and neglecting variations of the viscosity and the velocity-dependent dispersion I reduce the physical constants to one dimensionless parameter  $Ra$  – the Rayleigh number.

I consider a porous medium saturated with saline water with a uniform evaporation at the surface. This causes an increasing salt concentration near the surface and once saturation is reached there salt is accumulating and precipitating at the surface. Based on this I present an analytical solution of the transient from a constant background salinity to the steady state with saturated water at the top boundary to estimate the time to reach saturation.

The major theoretical result in chapter 3 of this thesis is the expansion of the linear stability analysis of Wooding, Homsy and van Dujin in [14–16] for small salinity perturbations with a horizontal wavenumber of  $a$ . Using a semi-analytical approach I am able to compute the neutral stability curves in parameter space  $Ra$ ,  $a$  and particularly the critical points  $Ra_c$ ,  $a_c$  for different top boundary conditions based on the approach of Wooding. The semi-analytical results are consistent with the results of Wooding and van Dujin. In addition to their work I compute the growth rate  $\Omega$  for different Rayleigh numbers as a function of the wavenumber and hence compute the most unstable wavenumber  $a(Ra)$ . This result helps to estimate the wavelength of early time perturbations from steady-state. In chapter 4 I present the results of the Hele-Shaw-geometry experiments conducted by Jana Lasser. I use quantities measured in these experiments to try and validate the results of my simulation later on. She measured the wavelength of the occurring convection cells as well as the front velocities as a function of the evaporation rate.

As a preparatory work for the numerical implementation of the two-dimensional salt playa model I firstly reproduce the numerical work of Rogerson and Meiburg in [17] in chapter 5. In contrast to our model they use double-periodic boundary conditions.

For those the computation of the Poisson equation can be done using a purely spectral method. To check the consistency of my implementation I compare the results qualitatively as well as quantitatively by using different measures such as the characteristic wavelength of occurring fingers and the growth rate of small perturbations. The wavelength is consistent with the most unstable mode compute in the linear stability analysis while the ratio of the front velocities and  $Ra - Ra_c$  are constant.

In chapter 6 I present the methods for the implementation of the actual two-dimensional model of salt-gradient driven convection in salt playa. I implement a system with constant evaporation rate at the top boundary as well as sinusoidal evaporation rate variations. I use a stream function-vorticity approach to simplify the equations and eliminate the pressure term. To compute the derivatives I use compact finite difference schemes of 6th order and I use a pseudo-spectral approach following [19–21] to solve the Poisson equation. I utilize an explicit multi-step, third-order Runge-Kutta scheme following [23]. By applying the theoretical results from the linear stability analysis I validate the implementation of the numerical simulation.

Utilizing this implementation I investigate the two-dimensional system in chapter 7: I analyze the wavelength as well as the front velocities of early time fingering behavior and compare the results with the most unstable mode from the theoretical analysis. The wavelengths are matching. Secondly I compute the regime of wavelengths in which stationary convection cells are stable as well as the front velocity at half height to validate the simulation with the non-dimensionalize experimental data. I analyze not the same regime for the height  $H$  regime as in experiments. Further investigation of the convection in regimes of larger heights  $H$  may help to explain the mismatch between experimental and numerical results. Besides it may be of interest to consider differential equations without neglecting the viscosity variations. Furthermore it is an open question why the experimental data are not all lying in the unstable regime of the linear stability diagram.

I use the properties of the real-world system and estimate the Rayleigh number in real world salt playa: The particle size is similar – based on measurements by Jana Lasse in the Death Valley and Owens Lake – and hence the permeability is in the same order of magnitude. Since the other physical constants are equivalent and the evaporation rate is much smaller in order of  $E_0 \approx 1 - 6 \times 10^{-10}$  m/s [1] the Rayleigh number is in order of  $Ra \approx 6000 - 36000$ . Since this Rayleigh number is much larger than the Rayleigh numbers in the experiments and the results of my numerical simulation I cannot give a robust estimation of length scales of the occurring subsurface convection cells in real world salt-playa.

The major result of the numerical simulations is the study of the subsurface convection

and the surface salt ridge patterns. Imposing sinusoidal evaporation rate variations I am able to show that the convection cells are pinned by such variations. I quantify the pinning efficiency as a function of Rayleigh number and amplitude of the variations. Hence, the patterns may pin the convection cells in real world salt playa if the surface patterns causes variations in the evaporation rate. This result makes our hypothesis for the driving mechanism of the salt polygon formulation more plausible, since the feedback mechanism is a crucial part of the hypothesis.



## A. Appendix

### References

- <sup>1</sup>S. Tyler, S Kranz, M. Parlange, J Albertson, G. Katul, G. Cochran, B. Lyles, and G Holder, "Estimation of groundwater evaporation and salt flux from owens lake, california, usa", *Journal of Hydrology* **200**, 110–135 (1997).
- <sup>2</sup>J. M. Nield, R. G. Bryant, G. F. Wiggs, J. King, D. S. Thomas, F. D. Eckardt, and R. Washington, "The dynamism of salt crust patterns on playas", *Geology* **43**, 31–34 (2015).
- <sup>3</sup>F. Christiansen, "Polygonal fracture and fold systems in the salt crust, great salt lake desert, utah", *Science* **139**, 607–609 (1963).
- <sup>4</sup>S. Lokier, "Development and evolution of subaerial halite crust morphologies in a coastal sabkha setting", *Journal of arid environments* **79**, 32–47 (2012).
- <sup>5</sup>L. F. Dellwig, "Significant features of deposition in the hutchinson salt, kansas, and their interpretation", *Geological Society of America Special Papers* **88**, 421–428 (1968).
- <sup>6</sup>R. M. Tucker, "Giant polygons in the triassic salt of cheshire, england: a thermal contraction model for their origin", *Journal of Sedimentary Research* **51** (1981).
- <sup>7</sup>B. Li, Y.-P. Cao, X.-Q. Feng, and H. Gao, "Mechanics of morphological instabilities and surface wrinkling in soft materials: a review", *Soft Matter* **8**, 5728–5745 (2012).
- <sup>8</sup>L. Goehring, "Evolving fracture patterns: columnar joints, mud cracks and polygonal terrain", *Phil. Trans. R. Soc. A* **371**, 20120353 (2013).
- <sup>9</sup>H. Eloukabi, N Sghaier, S. B. Nasrallah, and M. Prat, "Experimental study of the effect of sodium chloride on drying of porous media: the crusty–patchy efflorescence transition", *International Journal of Heat and Mass Transfer* **56**, 80–93 (2013).
- <sup>10</sup>B. Metz, O. Davidson, H. De Coninck, M. Loos, and L. Meyer, *Ipcc special report on carbon dioxide capture and storage*, tech. rep. (Intergovernmental Panel on Climate Change, Geneva (Switzerland). Working Group III, 2005).
- <sup>11</sup>J. J. Hidalgo, J. Fe, L. Cueto-Felgueroso, and R. Juanes, "Scaling of convective mixing in porous media", *Physical review letters* **109**, 264503 (2012).
- <sup>12</sup>A. Herbert, C. Jackson, and D. Lever, "Coupled groundwater flow and solute transport with fluid density strongly dependent upon concentration", *Water Resources Research* **24**, 1781–1795 (1988).
- <sup>13</sup>R. Wooding, S. W. Tyler, and I. White, "Convection in groundwater below an evaporating salt lake: 1. onset of instability", *Water Resources Research* **33**, 1199–1217 (1997).
- <sup>14</sup>R. Wooding, "Rayleigh instability of a thermal boundary layer in flow through a porous medium", *Journal of fluid mechanics* **9**, 183–192 (1960).
- <sup>15</sup>G. M. Homsy and A. E. Sherwood, "Convective instabilities in porous media with through flow", *AIChE Journal* **22**, 168–174 (1976).

- <sup>16</sup>C. Van Duijn, G. Pieters, R. Wooding, and A Van Der Ploeg, "Stability criteria for the vertical boundary layer formed by throughflow near the surface of a porous medium", *Environmental Mechanics: Water, Mass and Energy Transfer in the Biosphere: The Philip Volume*, 155–169 (2002).
- <sup>17</sup>A Rogerson and E Meiburg, "Numerical simulation of miscible displacement processes in porous media flows under gravity", *Physics of Fluids A: Fluid Dynamics* **5**, 2644–2660 (1993).
- <sup>18</sup>J. L. de Lagrange, "Lagrange mémoire sur la théorie du mouvement des fluides", *Nouv Mem de l'Acad de Sci de Berlin* **12**, 151–188 (1781).
- <sup>19</sup>M. Ruith and E. Meiburg, "Miscible rectilinear displacements with gravity override. part 1. homogeneous porous medium", *Journal of Fluid Mechanics* **420**, 225–257 (2000).
- <sup>20</sup>A Riaz and E Meiburg, "Three-dimensional miscible displacement simulations in homogeneous porous media with gravity override", *Journal of Fluid Mechanics* **494**, 95–117 (2003).
- <sup>21</sup>C.-Y. Chen, *Topics in miscible porous media flows* (University of Southern California, 1998).
- <sup>22</sup>S. K. Lele, "Compact finite difference schemes with spectral-like resolution", *Journal of computational physics* **103**, 16–42 (1992).
- <sup>23</sup>A. Wray, "Minimal storage time advancement schemes for spectral methods", NASA Ames Research Center, California, Report No. MS **202** (1990).
- <sup>24</sup>H. Darcy, "Les fontaines publique de la ville de dijon", Dalmont, Paris **647** (1856).
- <sup>25</sup>C. Soulaïne, *On the origin of darcy's law*, 2015.
- <sup>26</sup>D. A. Nield and A. Bejan, *Convection in porous media*, Vol. 3 (Springer, 2006).
- <sup>27</sup>C. T. Simmons, K. A. Narayan, and R. A. Wooding, "On a test case for density-dependent groundwater flow and solute transport models: the salt lake problem", *Water Resources Research* **35**, 3607–3620 (1999).
- <sup>28</sup>M. Muskat, "The flow of fluids through porous media", *Journal of Applied Physics* **8**, 274–282 (1937).
- <sup>29</sup>S. P. Neuman, "Theoretical derivation of darcy's law", *Acta Mechanica* **25**, 153–170 (1977).
- <sup>30</sup>K. Chamsri, "Derivation of darcy's law using homogenization method", *World Academy of Science, Engineering and Technology, International Journal of Mathematical, Computational, Physical, Electrical and Computer Engineering* **7**, 1399–1403 (2013).
- <sup>31</sup>S. Whitaker, "Flow in porous media i: a theoretical derivation of darcy's law", *Transport in porous media* **1**, 3–25 (1986).
- <sup>32</sup>U. Hornung, *Homogenization and porous media*, Vol. 6 (Springer Science & Business Media, 2012).
- <sup>33</sup>H. Brinkman, "A calculation of the viscosity and the sedimentation constant for solutions of large chain molecules taking into account the hampered flow of the solvent through these molecules", *Physica* **13**, 447–448 (1947).



- <sup>34</sup>E. Dufresne, E. Corwin, N. Greenblatt, J. Ashmore, D. Wang, A. Dinsmore, J. Cheng, X. Xie, J. Hutchinson, and D. Weitz, "Flow and fracture in drying nanoparticle suspensions", *Physical Review Letters* **91**, 224501 (2003).
- <sup>35</sup>R. C. Weast, *Crc handbook of chemistry and physics. cleveland, ohio*, 1977.
- <sup>36</sup>A. Pellew and R. Southwell, "On maintained convective motion in a fluid heated from below", in *Proceedings of the royal society of london a: mathematical, physical and engineering sciences*, Vol. 176, 966 (The Royal Society, 1940), pp. 312–343.
- <sup>37</sup>R. Askey and A. O. Daalhuis, "Generalized hypergeometric functions and meijer g-function", *NIST Handbook of Mathematical Functions*, Editors FWJ Olver, DW Lozier, RF Boisvert, CW Clark, US Department of Commerce, National Institute of Standards and Technology, Washington, DC, Cambridge University Press, Cambridge, 403–418 (2010).
- <sup>38</sup>J. W. Elder, "Steady free convection in a porous medium heated from below", *Journal of Fluid Mechanics* **27**, 29–48 (1967).
- <sup>39</sup>B. Thiede, *Experiments for the investigation of convection of salt water in porous media*, Bachelor's Thesis, 2016.
- <sup>40</sup>B. K. Hartline and C. Lister, "Thermal convection in a hele-shaw cell", *Journal of Fluid Mechanics* **79**, 379–389 (1977).
- <sup>41</sup>H. Lamb, *Hydrodynamics* (Cambridge university press, 1932).
- <sup>42</sup>G. Taylor, "Dispersion of soluble matter in solvent flowing slowly through a tube", in *Proceedings of the royal society of london a: mathematical, physical and engineering sciences*, Vol. 219, 1137 (The Royal Society, 1953), pp. 186–203.
- <sup>43</sup>D. R. Lide, *86th handbook of chemistry and physics*, 2006.
- <sup>44</sup>S. Ergun, "Fluid flow through packed columns", *Chem. Eng. Prog.* **48**, 89–94 (1952).
- <sup>45</sup>Z. Zeng and R. Grigg, "A criterion for non-darcy flow in porous media", *Transport in porous media* **63**, 57–69 (2006).
- <sup>46</sup>G. d. Josselin de Jong, "Singularity distributions for the analysis of multiple-fluid flow through porous media", *Journal of Geophysical Research* **65**, 3739–3758 (1960).
- <sup>47</sup>C. Tan and G. Homsy, "Simulation of nonlinear viscous fingering in miscible displacement", *The Physics of fluids* **31**, 1330–1338 (1988).
- <sup>48</sup>R. Courant, K. Friedrichs, and H. Lewy, "Über die partiellen differenzengleichungen der mathematischen physik", *Mathematische annalen* **100**, 32–74 (1928).
- <sup>49</sup>C. Tan and G. Homsy, "Stability of miscible displacements in porous media: rectilinear flow", *The Physics of fluids* **29**, 3549–3556 (1986).
- <sup>50</sup>J. G. Tyler, "Analysis and implementation of high-order compact finite difference schemes", (2007).
- <sup>51</sup>M. H. Carpenter, D. Gottlieb, and S. Abarbanel, "The stability of numerical boundary treatments for compact high-order finite-difference schemes", *Journal of Computational Physics* **108**, 272–295 (1993).

- <sup>52</sup>C. Canuto, M. Y. Hussaini, A. Quarteroni, A. Thomas Jr, et al., *Spectral methods in fluid dynamics* (Springer Science & Business Media, 2012).
- <sup>53</sup>C.-Y. Chen and E. Meiburg, “Miscible porous media displacements in the quarter five-spot configuration. part 1. the homogeneous case”, *Journal of Fluid Mechanics* **371**, 233–268 (1998).

## Figures

2.	Salt ridge patterns in the Death Valley. . . . .	6
3.	Sketch of the convection hypothesis. . . . .	7
4.	Two-dimensional slice of a porous medium. . . . .	10
5.	Density and viscosity as a function of salt concentration. . . . .	15
6.	Transient salinity before saturation at surface. . . . .	19
7.	Transient salinity at the surface. . . . .	19
8.	Most unstable mode of vertical salinity perturbation. . . . .	26
9.	Neutral stability curves and most unstable wavenumber. . . . .	27
10.	Growth rates as a function of wavenumber and Rayleigh number. . . . .	28
11.	Most unstable mode as a function of Rayleigh number. . . . .	28
12.	Experimental setup and measurement of wavelength and velocities. . . . .	30
13.	Experiment: Wavelength of cells as a function of the evaporation. . . . .	32
14.	Experiment: Maximal front velocities as a function of evaporation rate. . . . .	34
15.	Experiment: Difference of up- and downwelling front velocities. . . . .	34
16.	Sketch of flow configuration in Rogerson/Meiburg. . . . .	36
17.	Qualitative development of miscible displacement. . . . .	39
18.	Comparison of growth rates as a function of time. . . . .	40
19.	Comparison of growth rates as a function of wavenumber. . . . .	40
20.	Growth rates of salinity perturbations . . . . .	49
21.	Growth rates as a function of wavenumber. . . . .	50
22.	Qualitative development from steady-state to convection cells. . . . .	55
23.	Fingering for $Ra = 200$ and horizontal velocity profile. . . . .	56
24.	Wavenumber of the fingers as a function of the Rayleigh number. . . . .	57
25.	Front velocities of the fingering as a function of Rayleigh number. . . . .	57
26.	Relative front velocities of the fingering as a function of Rayleigh number. . . . .	58
27.	Exemplary convection cell. . . . .	60
28.	Wavelength regime for stationary convection cells. . . . .	61
29.	Front velocities of stable convection cells for different wavelengths. . . . .	61
30.	Maximal velocities of convection cells for various Rayleigh numbers. . . . .	62
31.	neutral stability curve and experimental wavelengths of convection . . . . .	64
32.	Comparison of stationary wavelength regime and experiment . . . . .	65
33.	Comparison of experimental front velocity and simulation. . . . .	65
34.	Variations in evaporation rate for pinning study. . . . .	66
35.	Phase shift of convection cell to imposed evaporation. . . . .	67
36.	Phase of convection cell to imposed evaporation as a function of time. . . . .	68
37.	Pinning efficiency as a function of Rayleigh number. . . . .	69
38.	Stationary wavelength regimes with evaporation rates variations. . . . .	70

# Acknowledgements

My master thesis was supervised by Dr. Lucas Goehring and his doctoral student Jana Lasser. I am very grateful for the good collaboration and the opportunity to work on the understanding of polygonal patterns in salt playa.

Lucas and Jana gave me many insights in the methodology of good scientific practice and research. They provided helpful advice throughout my thesis and discussed occurring problems regarding the theoretical and numerical work. I thank Jana for providing experimental data as well as results from her field trip to Owens Lake.

I am grateful for the helpful suggestions for the linear stability analysis from Antoine Fourrière, Stephan Herminghaus, Jana Lasser and Lucas Goehring as well as the advices regarding the simulation given by Fabian Schwarzendahl and Marco Mazza.

Additionally I am grateful to Thomas Eggers for taking care of my IT problems and remotely helping to print a conference poster in the late evening. I am grateful for the patience of Monika Teuteberg while doing all the necessary paper work.

I would like to thank the whole working groups of Lucas Goehring and Marco Mazza for their good company and the enjoyable working atmosphere at the institute. I appreciated the discussions with them concerning politics, physics as well as other topics and spending free time together.

Finally, I thank my family for their manifold support during the thesis period.

**Erklärung**

nach §13(8) der Prüfungsordnung für den Bachelor-Studiengang Physik und den Master-Studiengang Physik an der Universität Göttingen:

Hiermit erkläre ich, dass ich diese Abschlussarbeit selbständig verfasst habe, keine anderen als die angegebenen Quellen und Hilfsmittel benutzt habe und alle Stellen, die wörtlich oder sinngemäß aus veröffentlichten Schriften entnommen wurden, als solche kenntlich gemacht habe.

Darüberhinaus erkläre ich, dass diese Abschlussarbeit nicht, auch nicht auszugsweise, im Rahmen einer nichtbestandenenen Prüfung an dieser oder einer anderen Hochschule eingereicht wurde.

Göttingen, den 29. September 2017

(Marcel Ernst)